Observations of Middle Atmosphere CO from the *UARS* ISAMS during the Early Northern Winter 1991/92

D. R. ALLEN,*,## J. L. STANFORD,* M. A. LÓPEZ-VALVERDE,+ N. NAKAMURA,# D. J. LARY,@ A. R. DOUGLASS,& M. C. CERNIGLIA,** J. J. REMEDIOS,++ AND F. W. TAYLOR++

* *Department of Physics and Astronomy, Iowa State University, Ames, Iowa*
+ *Instituto de Astrofísica de Andalucía, Granada, Spain*
# *Department of Geophysical Sciences, University of Chicago, Chicago, Illinois*
@ *Department of Chemistry, Centre for Atmospheric Science, Cambridge University, United Kingdom*
& *NASA/Goddard Space Flight Center, Greenbelt, Maryland*
** *Applied Research Corporation, Landover, Maryland*
++ *Department of Physics, Oxford University, Oxford, United Kingdom*

(Manuscript received 28 July 1997, in final form 28 April 1998)

ABSTRACT

Structure and kinematics of carbon monoxide in the upper stratosphere and lower mesosphere (10–0.03 hPa) are studied for the early northern winter 1991/92 using the Upper Atmosphere Research Satellite Improved Stratospheric and Mesospheric Sounder (ISAMS) measurements. The study is aided by data from a 6-week parameterized-chemistry run of the Goddard Space Flight Center 3D Chemistry and Transport Model (CTM), initialized on 8 December 1991.

Generally, CO mixing ratios increase with height due to the increasing source contribution from CO_2 photolysis. In the tropical upper stratosphere, however, a local maximum in CO mixing ratio occurs. A simple photochemical model is used to show that this feature results largely from methane oxidation.

In the extratropics the photochemical lifetime of CO is long, and therefore its evolution is dictated by large-scale motion of air, evidenced by strong correlation with Ertel potential vorticity. This makes CO one of the few useful observable tracers at the stratopause level and above. Thus CO maps are used to study the synoptic evolution of the polar vortex in early January 1992.

Modified Lagrangian mean mixing diagnostics are applied to ISAMS and CTM data to examine the strength of the mixing barrier at the polar vortex edge. It is demonstrated that planetary wave activity weakens the barrier, promoting vortex erosion. The vortex erosion first appears in the lower mesosphere and subsequently descends through the upper stratosphere, and is attributed to effects of planetary wave dissipation.

Agreement between ISAMS and CTM is good in the horizontal distribution of CO throughout the examined period, but vertical CO gradients in the CTM weaken with time relative to the ISAMS observations.

1. Introduction

The major source of CO in the upper middle atmosphere (mesosphere and lower thermosphere) comes from CO_2 photolysis (see Fig. 1):

$$CO_2 + h\nu \rightarrow CO + O. \quad (1)$$

Generally, CO mixing ratios increase with height throughout the middle atmosphere due to the high altitude source and downward advective and diffusive flux into the mesosphere and stratosphere. Methane oxidation plays a large role in the stratospheric budget, providing a CO source that maximizes near 30 km; although some CO molecules produced from combustion and natural sources near the surface reach the stratosphere, most are destroyed in the troposphere (Brasseur and Solomon 1986). The only major CO chemical loss mechanism in the middle atmosphere is oxidation by the hydroxyl radical (OH) to CO_2:

$$CO + OH \rightarrow CO_2 + H, \quad (2)$$

which occurs during the sunlit hours, since OH is produced from photolysis reactions (e.g., with H_2O). In the thermosphere chemical loss is negligible resulting in a downward flux of CO into the mesosphere (Allen et al. 1981).

In the upper stratosphere and mesosphere, the photochemical lifetime of CO is on the same order (weeks to months) as vertical transport timescales and is gen-

Current affiliation: Department of Geophysical Sciences, University of Chicago, Chicago, Illinois.

Corresponding author address: Dr. Douglas Allen, Department of Geophysical Sciences, University of Chicago, 5734 S. Ellis Ave., Chicago, IL 60637.
E-mail: drallen@bethel.uchicago.edu

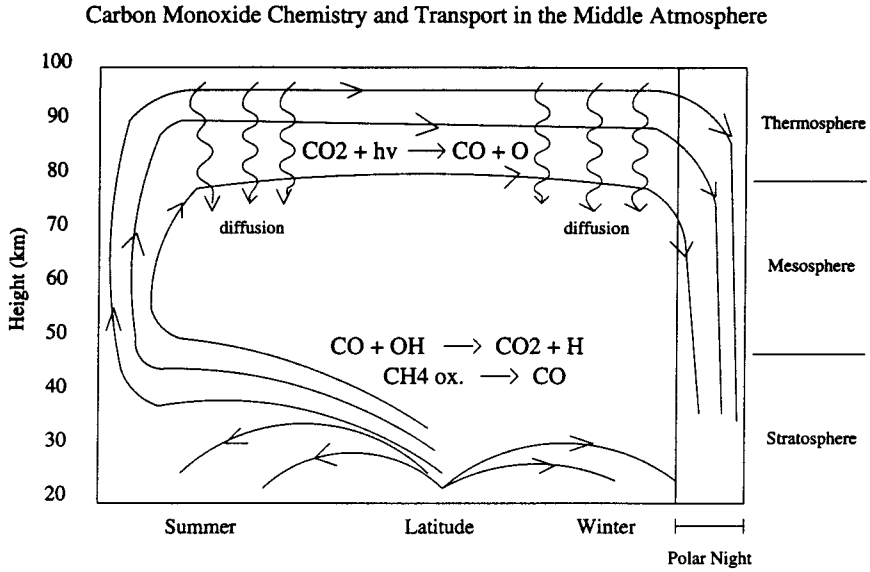

FIG. 1. Schematic diagram of CO chemistry and transport processes in the meridional plane under solstice conditions, adapted from Solomon et al. (1985).

erally larger than horizontal transport timescales (days to weeks), making it a useful tracer of the atmospheric transport (Hays and Olivero 1970; Wofsy et al. 1972; Allen et al. 1981; Solomon et al. 1985). In the polar night, stratospheric and mesospheric CO is conserved due to the lack of OH, so it should be a particularly good tracer of winter polar vortex dynamics.

Early predictions of the CO mixing ratio in the middle atmosphere were made by Hays and Olivero (1970), who incorporated CO and CO_2 photochemistry and vertical transport in a 1D model to calculate mixing ratio profiles from 0 to 200 km for two recombination regimes and three eddy diffusion formulations. They found that CO mixing ratios increase with height throughout the middle atmosphere due to CO_2 photolysis reaching at least 30 ppmv in the thermosphere. Wofsy et al. (1972) and Wofsy (1976) furthered this work by including more complex photochemistry and quantified the importance of CO_2 photolysis, CH_4 oxidation, and loss from OH for the CO distribution.

A pioneering study of CO in the middle atmosphere by Solomon et al. (1985) used a 2D chemistry and transport model from 10 to 116 km to examine the distribution and seasonal evolution of CO. Salient points from the study include: 1) CO mixing ratios increase with height throughout most of the middle atmosphere; 2) mesospheric CO abundances are larger in winter than in summer due to vertical advective transport; 3) extremely large CO mixing ratios are found in the polar night mesosphere–upper stratosphere due to diabatic descent and lack of OH, with especially sharp CO gradients occurring at the polar night terminator; 4) midlatitudes may exhibit significant CO variability during periods of large-amplitude planetary waves.

Carbon monoxide mixing ratios in the middle atmosphere have been previously measured mainly by ground-based microwave techniques (Waters et al. 1976; Goldsmith et al. 1979; Kunzi and Carlson 1982; Clancy et al. 1982, 1984; Bevilacqua et al. 1985; Aellig et al. 1995). These studies have shown the general tendency of CO mixing ratios to increase with altitude and become larger in the winter hemisphere and propose that chemical as well as dynamical processes such as planetary wave activity (Bevilacqua et al. 1985), gravity wave activity (Aellig et al. 1995), vertical and horizontal mixing, and interhemispheric circulations in the middle atmosphere, contribute to large CO variability on timescales of days to years.

Satellite observations of infrared CO emission by the Stratospheric and Mesospheric Sounder (SAMS) instrument onboard *NIMBUS-7* were obtained from the fundamental vibrational–rotational band at 4.6 μm (Murphy 1985). The SAMS CO indicated large variability with altitude, latitude, and time in the middle atmosphere, as expected from model predictions (Solomon et al. 1985). Carbon monoxide measurements in the middle atmosphere have also been made by infrared occultation instruments on various shuttle missions (Girard et al. 1988; Gunson et al. 1990; Rinsland et al. 1992; Gunson et al. 1996; Chang et al. 1996).

Carbon monoxide observations have also been obtained from the Improved Stratospheric and Mesospheric Sounder (ISAMS) onboard the Upper Atmosphere Research Satellite (UARS). This instrument provides nearly global coverage with good vertical resolution to examine the CO distribution from approximately 10 to 0.03 hPa (roughly 30–70 km). Preliminary zonal-mean maps of ISAMS CO were presented in López-Valverde

et al. (1993) and a more detailed discussion of the seasonal zonal-mean evolution was described in López-Valverde et al. (1996). A detailed comparison with atmospheric tracer molecular spectroscopy CO data is presented in López-Valverde et al. (1998).

The present study examines ISAMS CO (data description provided in section 2) during the early northern winter 1991/92. ISAMS CO data are compared with output from a parameterized-chemistry run of the Goddard Space Flight Center (GSFC) 3D Chemistry and Transport Model (CTM). The CTM is described in section 3 of this paper. Section 4 introduces two Lagrangian diagnostic schemes that are applied to ISAMS and CTM data. Section 5 contains the data analysis. First, the meridional distribution of ISAMS CO is discussed, followed by an explanation of the local maximum in the tropical upper stratosphere. Next, the synoptic evolution of the polar vortex in early January 1992 is presented, using CO as a dynamical tracer. A comparison of ISAMS and CTM CO is made by examining the synoptic evolution and zonal-mean meridional structure. Finally, modified Lagrangian mean diagnostics are used to study horizontal mixing processes during the vortex dissipation occurring in January 1992. Section 6 contains a summary of significant points.

2. Data description

This study examines version 12 CO data from the ISAMS, one of the 10 UARS instruments. ISAMS measures the CO concentration in the upper stratosphere and mesosphere by detecting infrared limb emission from the vibrational–rotational band near 4.6 μm. The CO signal is contaminated by emissions from other constituents, mainly N_2O, CO_2, and O_3. Although pressure modulation techniques (see Taylor et al. 1993) help to discriminate between closely spaced or overlapping emission lines, contamination is still a major concern in the CO retrieval (López-Valverde et al. 1996).

Another difficulty in the retrieval is that CO is not in local thermodynamic equilibrium (non-LTE) in most of the middle atmosphere (López-Valverde et al. 1991; López-Puertas et al. 1993). In non-LTE conditions thermodynamic equilibrium is not met and therefore the population of the emitting level does not follow the Boltzmann distribution. In this case the source function for the given transition must be used in the retrieval rather than the Planck function. The non-LTE model used in the ISAMS retrieval is described by López-Puertas et al. (1993) and López-Valverde et al. (1996).

ISAMS CO retrievals are performed from approximately 10 to 0.03 hPa. At pressures higher than 10 hPa the signal is significantly contaminated by Pinatubo aerosols. One criterion used for judging the quality of the retrieved measurements is the ratio of the retrieved variance to a priori variance. When this ratio exceeds 2 the data quality (denoted Q here) is flagged by setting it negative. At this point, the data contain equal information from the measurements and a priori climatology, which for version 12 ISAMS CO is a seasonally varying zonal-mean field, derived from a blended dataset of GSFC 2D model output and version 10 ISAMS CO.

This study uses level 2 and level 3AT (described below) CO from ISAMS processing version 12, the most recent processing version, which has not yet been fully validated (preliminary error estimates are on the order of 30% for individual measurements). Version 12 CO has several improvements over the previously validated version 10 (see López-Valverde et al. 1996), including inline non-LTE source function calculation rather than tabulated source function and use of ISAMS N_2O to remove contamination rather than a 2D climatology. Level 2 refers to the first retrieved data product arranged as consecutive vertical profiles, which are positioned along the satellite limb track at regular time intervals, but irregularly spaced in the vertical. Level 3AT is a standard UARS format produced by interpolating level 2 data horizontally along the limb track to equally spaced times ($\sim$65 s) and vertically to standard UARS pressure surfaces. ISAMS measures with twice the horizontal sampling rate of the level 3AT output, so the interpolation from level 2 to level 3AT involves a roughly 50% decrease in the horizontal resolution.

Figure 2 provides the distribution of good quality ($Q > 0$) CO measurements for 12 January 1992, along with Ertel potential vorticity derived from National Centers for Environmental Prediction (NCEP) meteorological analyses at eight nearby potential temperature surfaces (data provided by G. Manney). Here level 3AT data in the Northern Hemisphere are plotted at 16 pressure levels from 10 to 0.032 hPa. Each colored circle marks one level 3AT measurement with the color representing the $\log_{10}$ of the CO mixing ratio in ppmv. Data flagged with negative Q are not plotted, resulting in gaps in Fig. 2. For example, in part of the displaced polar vortex (as identified by the PV contours) at 4.642 hPa the CO data are flagged as ''poor,'' even though CO mixing ratios in the polar vortex are expected to be large (as will be explained later) and therefore may be expected to provide sufficient radiance to make a reliable measurement. However, by comparing these plots with ISAMS temperature distributions (not shown here) it was found that a strong zonally asymmetric (wave 1) temperature pattern is present with a maximum displaced slightly west (clockwise) of the PV maximum. It is likely that the low temperatures offset the high CO mixing ratios, making the radiance measured in this region by ISAMS too small to make an accurate retrieval. Large regions of poor data are found above 0.1 hPa due to excessive noise in the measured radiances. Only limited nighttime data are available in the mesosphere, whereas solar non-LTE pumping allows for reliable daytime mesospheric retrievals (López-Valverde et al. 1996).

Gridded ISAMS CO used in this study were produced from level 2 data by first interpolating vertically in log pressure coordinates at each lat–long point to a given

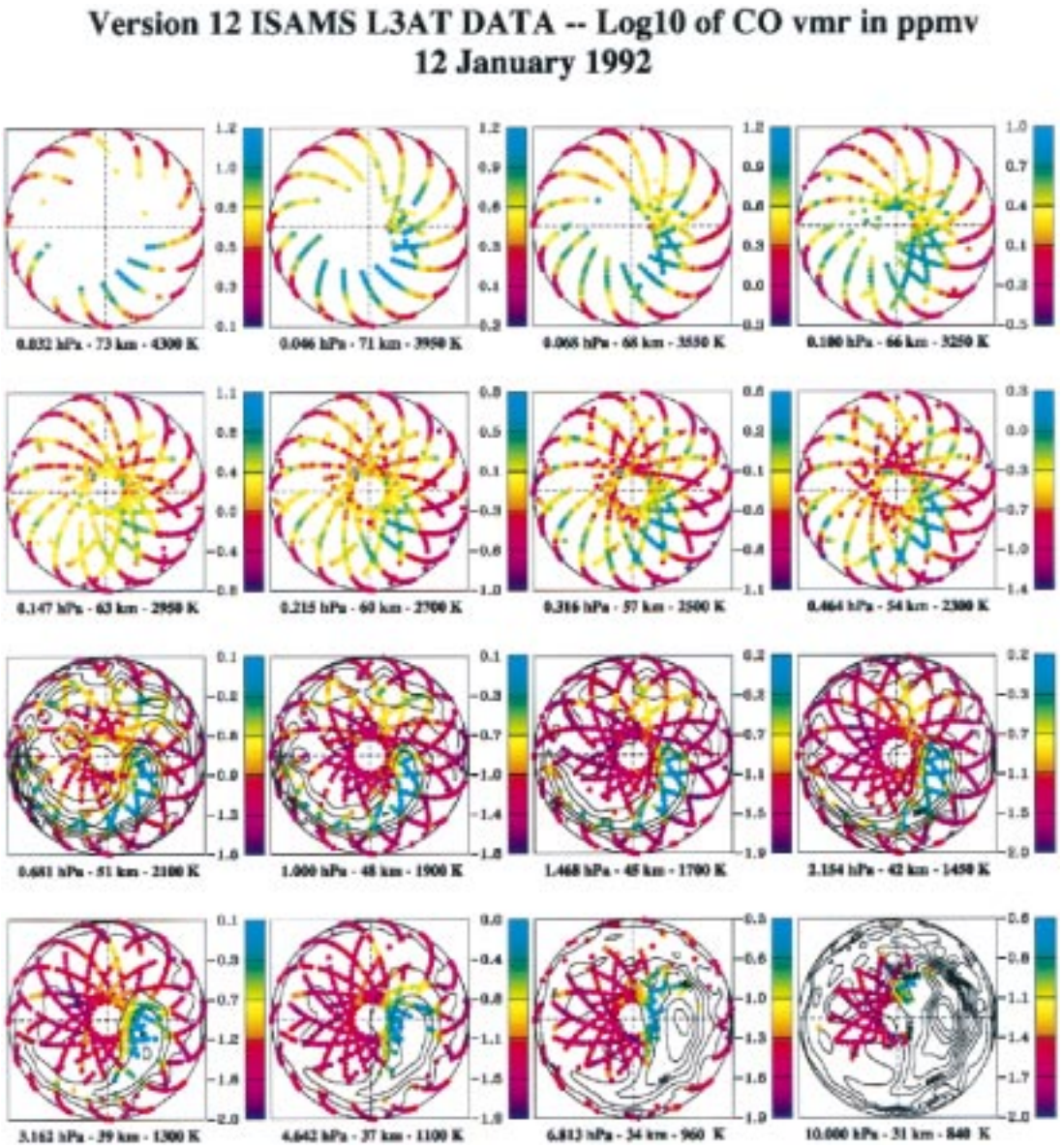

FIG. 2. Version 12 ISAMS CO at 16 pressure levels on 12 January 1992. Each colored circle represents one observation on the UARS level 3AT grid. The color bar for each level is the $\log_{10}$ of the CO mixing ratio in ppmv. Data flagged as ''poor'' by the retrieval are not included in the plot. The lowest eight levels are overlaid by contours of NCEP-derived PV on the potential temperature surfaces indicated. Nominal altitudes are provided for each pressure level. Projection is orthographic with 0° (180°) long on the right (left) side.

pressure grid (the same grid used by the CTM discussed below). At each pressure level the data were interpolated horizontally to a 2° lat × 5° long grid using a triangular interpolation routine. To ensure nearly hemispheric coverage of gridded CO, all data were used in the gridding, even data flagged as ''poor.'' A comparison of zonal-mean maps made with and without data flagged by negative Q show only small differences, none of which affect any of the conclusions made in this paper. This procedure also does not adversely affect the horizontal maps at 1 hPa presented in this paper, since most of the level 2 data points at that pressure have positive Q (see Fig. 2). Regions of missing data (largely 80°–90°N, beyond the viewing geometry of *UARS*) were filled with CTM CO scaled by the ratio of the zonal-mean ISAMS CO to CTM CO at 78°N. A nine-point (three lat points × three long points) average was applied to the subsequent data both to ease the transition from ISAMS to CTM CO at 80°N and to reduce random variability from instrument noise. No effort was made in this gridding to account for the asynoptic sampling of the ISAMS data.

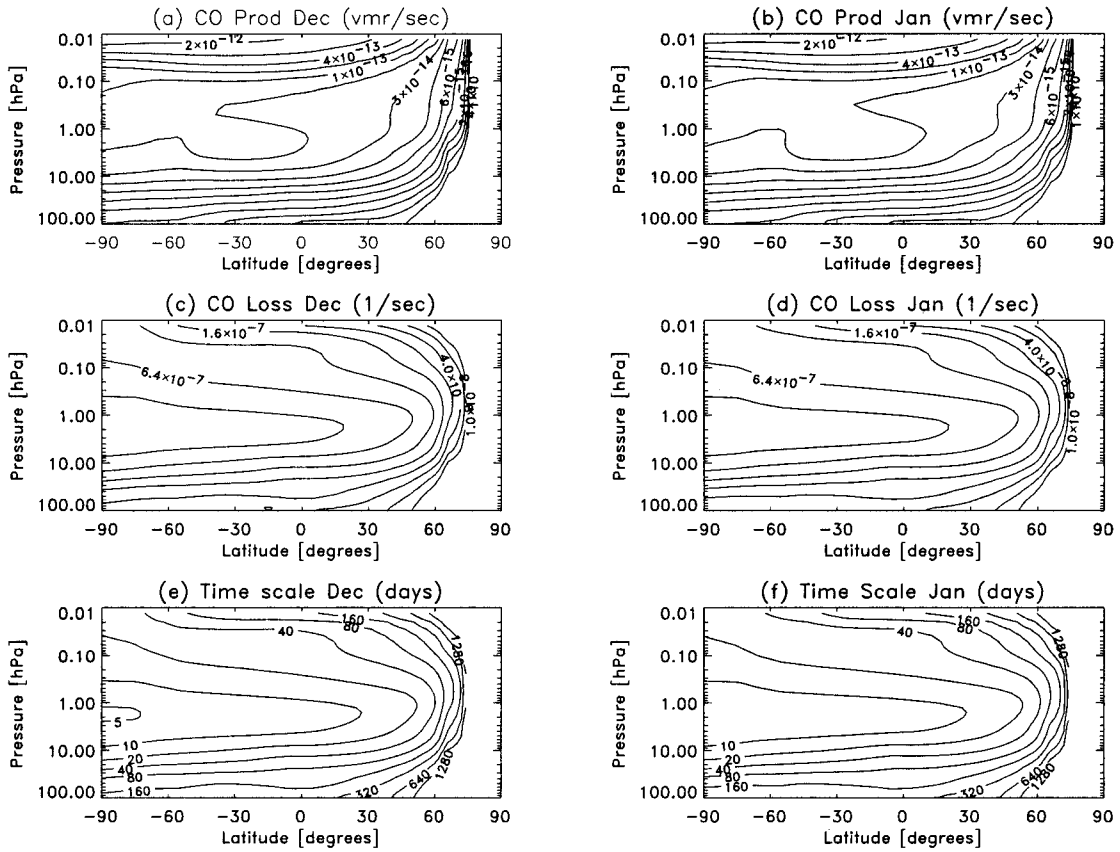

FIG. 3. The CO *P* (production) (a), (b) and *L* (loss) (c), (d) terms used for the GSFC 3D CTM run analyzed in this study. These terms [taken from model described in Fleming et al. (1995)] are monthly and zonal means for December 1991 and January 1992. Also plotted (e), (f) are the photochemical timescales (in days) computed by 1/*L*.

3. Model description

This study compares ISAMS CO with CO distributions simulated by the GSFC 3D CTM [see Douglass et al. (1996) for a complete model description]. For the model run presented here, the full-chemistry was not used, but was substituted with monthly mean parameterized photochemical production (*P*) and loss (*L*) for CO, CH_4, and N_2O (the chemical source in the tracer continuity equation is given by $P - \chi L$, where χ is the mixing ratio of the given tracer).

The wind fields used to drive the CTM are taken from an advanced version of the Goddard Earth Observing System (GEOS-1) assimilation (Schubert et al. 1993), which incorporates changes in the modeling component of the GEOS-1 assimilation system. These changes include a new radiation scheme, orographic gravity wave drag, a rotated pole to remove the pole singularity, and 70 sigma levels from the surface to 0.01 hPa. The algorithms are described in DAO (1996). This is the model that will be part of the new GEOS system scheduled to start production in 1998. Horizontal winds are taken from this offline assimilation and vertical winds are calculated internally in the CTM; numerical transport within the CTM is calculated using the piecewise parabolic scheme of Lin and Rood (1996). The CTM does not parameterize unresolved (subgrid-scale) turbulence. The model top (0.01 hPa) and surface (1000 hPa) are constrained by zero vertical velocity.

The monthly mean photochemical production and loss terms are taken from an older version of the the GSFC 2D model (Fleming et al. 1995). Figure 3 shows the December and January CO *P* and *L* terms used by the model. The large production rates above 0.1 hPa are due to CO_2 photolysis, whereas small production and loss rates occur in the polar night (*P* and *L* are set to zero poleward of 76°N). The loss rates decrease with latitude from the summer to winter pole and maximize near the stratopause (~1 hPa). Also shown in Fig. 3 is the chemical timescale (in days) calculated from the loss rates (timescale = 1/*L*) for December and January. The timescale varies from several days near the summer polar stratopause to several years in the high northern latitudes, where the CO mixing ratio should behave as a conserved tracer.

The CTM was initialized with CO, CH_4, and N_2O on 8 December 1991 using a potential vorticity (PV)/potential temperature mapping scheme (Lary et al. 1995) incorporating meteorological data from the GSFC DAO

along with ISAMS CO and cryogenic limb array etalon spectrometer N_2O and CH_4. Regions of missing data were filled with output from the GSFC 2D model. In addition, a completely passive tracer ($P = 0$; $L = 0$) was introduced that was initialized identically to CO. The model run was from 8 December 1991 to 18 January 1992, with output once per day at 0000 UTC on a 2° lat × 2.5° long grid.

4. Analysis techniques: PV mapping and MLM diagnostics

A fundamental shift in descriptions of atmospheric dynamics is occurring as Lagrangian analyses are replacing conventional Eulerian analyses. This shift has been facilitated by the production of relatively high-resolution isentropic PV maps. A technique, denoted here as ''PV-mapping,'' is becoming an increasingly popular diagnostic tool for analyzing atmospheric chemical transport. PV-mapping involves averaging constituent mixing ratios along PV contours on isentropic surfaces (i.e., surfaces of constant potential temperature, θ) to produce 2D maps in PV and θ coordinates. This procedure effectively accounts for reversible (and resolvable) wave motions that can cause confusion in zonal-mean analyses. PV-mapping has proved to be quite useful for analyzing constituent transport, especially in the polar stratosphere, and for constructing constituent distributions from limited observations (e.g., Schoeberl et al. 1989).

PV-mapping basically involves a transformation of the tracer continuity equation to conservative coordinates (Schoeberl and Lait 1991). Potential temperature is chosen as the vertical coordinate, and PV, which is conserved for adiabatic, frictionless motion, is used in the horizontal. To the extent that both the constituent mixing ratio and PV are conserved, the two quantities will maintain a close correlation. As nonconservative processes (diabatic heating, friction, mixing, or photochemical effects) become important, the close correlation will be lost. For the PV-mapping in this study, PV on isentropic surfaces, derived from U.K. Meteorological Office (UKMO) meteorological analyses, is first converted to equivalent latitude, the latitude of a zonal circle centered at the pole that encompasses the same area as a given PV contour (see Lary et al. 1995). This equivalent latitude is then interpolated to the (lat–long pressure) locations of the ISAMS level 2 measurements thereby associating each ISAMS observation with a PV-derived equivalent latitude. Similarly, potential temperature is calculated from UKMO data and interpolated to the ISAMS level 2 measurement locations. This results in a series of points with coordinates (equivalent latitude, potential temperature, CO mixing ratio). The mixing ratios are then binned every 5° in equivalent latitude and 50 K in potential temperature, averaged, and smoothed with a nine-point (three equivalent latitude points by three potential temperature points) average to further remove instrument noise. To avoid errors from climatological bias and day/night differences in the retrieval, only daytime data with $Q > 0$ were used in the PV-mapping. The resulting map for 12 January 1992 is examined in section 5a.

As we shall see, one of the most dramatic aspects of the CO during the observed period is rapid horizontal distortion of isopleths and subsequent mixing. Here we diagnose horizontal mixing using the modified Lagrangian mean (MLM) technique. The theoretical basis of the method, which originated with McIntyre (1980), has recently been developed further by Nakamura (1995, 1996, 1998). In MLM, the tracer transport is measured with respect to a moving air mass instead of geographically fixed coordinates. Here the air mass is defined by the isosurfaces of tracer rather than PV. To the extent the tracer is conservative, the tracer isosurfaces are material surfaces so there is no ''leakage'' of substance, or there is no transport. As such, all transport in the MLM formalism comes from nonconservative processes including mixing, diabatic heating, and photochemistry. Although the full formulation (Nakamura 1995, 1998) encompasses all these effects, in the present paper we concentrate on isentropic mixing.

The key diagnostic is L_e, or the *equivalent length* of the tracer contour on the isentropic surface (Nakamura 1996). Suppose the short-term isentropic kinematics of tracer mixing ratio χ is well approximated by the simple advection–diffusion equation:

$$\frac{\partial \chi}{\partial t} + J(\Psi, \chi) = D\nabla^2\chi \tag{3}$$

where Ψ is the streamfunction, J is the Jacobian, and ∇^2 is the Laplacian. Here D is assumed constant and parameterizes all subgrid-scale mixing. Nakamura (1996, 1998) shows that Eq. (3) can be transformed to a one-dimensional diffusion equation

$$\frac{\partial}{\partial t}\chi(A, t) = \frac{\partial}{\partial A}\left(DL_e^2\frac{\partial \chi}{\partial A}\right) \tag{4}$$

using A, the area enclosed by the tracer contour, as the horizontal coordinate. Here

$$\begin{aligned} L_e^2(A, t) &= (\partial\chi/\partial A)^{-2}\frac{\partial}{\partial A}\mathcal{A}(|\nabla\chi|^2) \\ &= (\partial\chi/\partial A)^{-2}\langle|\nabla\chi|^2\rangle \end{aligned} \tag{5}$$

defines the square of the equivalent length, where the operator $\mathcal{A}(\cdot) = \int\int(\cdot)\,dA$ denotes the integral of a scalar over the area bounded by a χ contour; for example, $A = \mathcal{A}(1)$, and the operator $\langle\cdot\rangle = \partial\mathcal{A}(\cdot)/\partial A$ represents the contour average (Nakamura 1998). The quantity L_e is, to a good approximation, the perimeter length of the tracer contour enclosing area A [it reduces to the actual contour length when $|\nabla\chi|$ is constant around the contour], and hence measures the degree of scrambling by the flow (Nakamura 1998). It is clear from

Eq.(4) that DL_e^2 serves as an ''effective horizontal diffusivity'' (a Lagrangian equivalent of K_{yy}) and hence the drive for the tracer distribution in the area coordinate. Notice that although microscale mixing D is crucial, its effect is magnified by L_e^2 so the effective diffusivity is large when the tracer is well scrambled. Aside from the uncertainty in D at a given resolution, the effective diffusivity is precise and in principle computable from the instantaneous tracer distribution alone without resorting to particle advection. This is an advantage for tracer transport diagnosis in the middle atmosphere where wind observation is not readily available. Nakamura (1996) and Nakamura and Ma (1997) show that the diagnostic is resolution-sensitive quantitatively but not qualitatively.

In this paper we calculate L_e^2 by evaluating Eq. (5) literally using area averaging rather than contour averaging [the first equality in Eq. (5), see Nakamura and Ma (1997) for more details] and display it in a normalized form $\xi = \ln(L_e^2/L_o^2)$ where $L_o = 2\pi a \cos\phi_e$ is the circumference of the zonal circle at latitude ϕ_e, the equivalent latitude defined by $A(\chi, t) = 2\pi a^2(1 - \sin\phi_e)$, where a is the earth's radius. Thus ξ measures how much the tracer contour is stretched from a zonal circle, and vanishes when the tracer is perfectly zonal. Here L_e^2 is calculated on pressure surfaces here for convenience, rather than isentropic surfaces; the difference is small in the regions of interest.

5. Results

a. Meridional structure

The map of ISAMS CO for 12 January 1992 (Fig. 4a), constructed using the PV-mapping technique described in the previous section, provides a wealth of information about the transport and chemistry of CO in the middle atmosphere. Mixing ratios generally increase with potential temperature except from 30°N to 40°S equivalent latitude, below 1800 K (note: the $\log_{10}$ of the mixing ratio in ppmv is plotted in Fig. 4). Winter polar descent, bringing CO-rich air downward, is suggested by the high CO mixing ratios poleward of 50°N equivalent latitude [CO in the winter polar region is also enhanced due to lack of OH, which provides the main CO sink (Solomon et al. 1985)]. The CO mixing ratio increases by an order of magnitude between 30° and 80°N equivalent latitude over the potential temperature range 1200–1800 K. The large mesospheric CO mixing ratios appear to reach 1000 K (~35 km). There are few ISAMS observations with $Q > 0$ below 1000 K, and therefore the sharp vertical gradient at high equivalent latitudes between 800 and 1000 K does not necessarily denote the lower boundary of diabatic descent.

CO mixing ratios decrease from high to low northern equivalent latitudes in the mesosphere (above ~1900 K), whereas in the stratosphere near 1500 K minima are found near 20°N and 30°S equivalent latitude with a local maximum near 5°S. This feature persists without much change throughout November and December 1991 and January 1992. A similar map of N_2O (Fig. 4b) displays monotonically increasing mixing ratios from high to low equivalent latitudes as expected for a long-lived tracer with tropospheric source advected by the mean meridional circulation. The contrast between the CO and N_2O contours in the Tropics suggests that photochemistry is likely causing the tropical CO maximum. Section 5b examines this feature in detail, arguing that the low latitude CO maximum is due largely to methane oxidation.

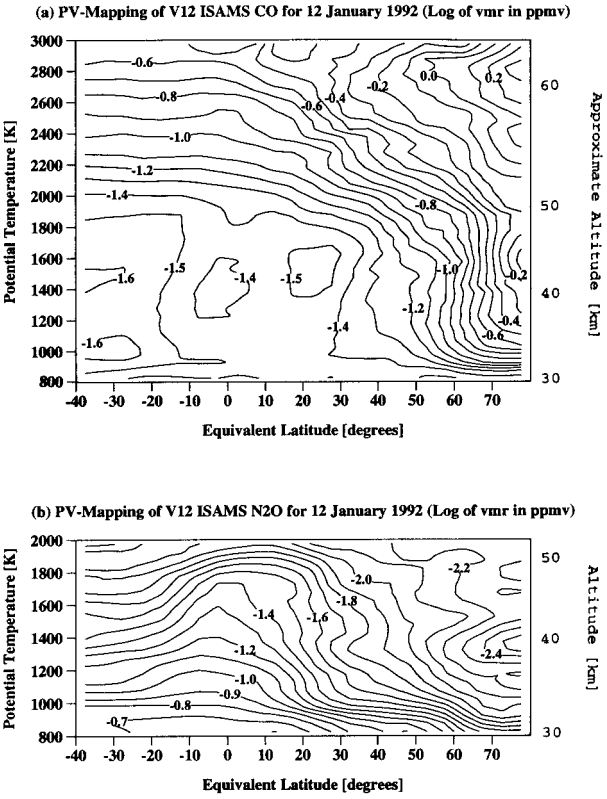

FIG. 4. (a) Potential vorticity (converted to equivalent latitude)–potential temperature map of ISAMS CO for 12 January 1992, made with UKMO temperatures and UKMO-derived PV. Only daytime data with good quality (as identified by the quality factor in the retrieval) were used in this analysis. Units are log (base 10) of the mixing ratio in ppmv. (b) Same as (a) but for ISAMS N_2O [note the difference in extent of the vertical scales in (a) and (b)].

b. Evidence of CH_4 oxidation in the upper stratosphere

The amount of CO produced from CH_4 oxidation in the upper stratosphere can be estimated by assuming a first-order balance between the following two reactions:

$$OH + CH_4 \rightarrow CH_3 + H_2O \ (k_1) \Rightarrow CO, \qquad (6)$$

$$OH + CO \rightarrow CO_2 + H \ (k_2). \qquad (7)$$

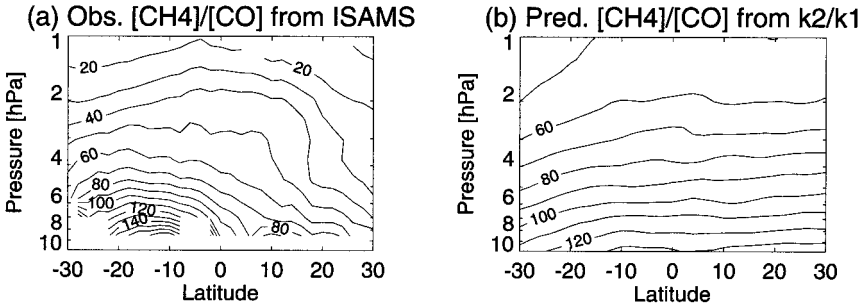

FIG. 5. (a) Zonal-mean $[CH_4]/[CO]$ ratio as observed from ISAMS V12 data for 1 January 1992. (b) The predicted $[CH_4]/[CO]$ ratio for 1 January 1992 as calculated from Eq. (9) using reaction rates from DeMore et al. (1997) and temperatures from the GSFC DAO assimilation.

Here we assume efficient (100%) conversion from CH_4 to CO in the upper stratosphere through the reaction given in Eq. (6) and neglect CH_4 loss from O^1D and Cl. As will be shown below, this provides a fairly good (within a factor of 2) approximation of the CO produced from CH_4 loss processes. Equations (6) and (7) represent one source and one sink of CO, which if balanced, provide the $[CH_4]/[CO]$ ratio:

$$\frac{[CH_4]}{[CO]} = \frac{k_2}{k_1}. \tag{8}$$

Figure 5a shows the observed zonal mean $[CH_4]/[CO]$ in the upper stratosphere from 30°S to 30°N for 1 January 1992 as calculated from ISAMS version 12 data, whereas Fig. 5b shows the predicted ratio from Eq. (8) using reaction rates from DeMore et al. (1997) and temperatures from the DAO assimilation. The observed and predicted ratio isopleths show similar slopes from 5 to 2 hPa for the region 30°S to the equator. North of 10°N, the observed ratio decreases rapidly with latitude, whereas the predicted ratio remains nearly constant with latitude from 10°S to 30°N. The Northern Hemisphere discrepancy is likely due to large meridional excursions of vortex air to low latitudes observed on this day (see Fig. 12a). Since the CO mixing ratio varies by an order of magnitude inside and outside the vortex, even localized regions of vortex air can cause large perturbations in the zonal-mean CO.

To estimate the relative contributions from chemistry and transport, we obtained chemical loss and transport timescales for CO from the GSFC 2D CTM (Jackman et al. 1996) for the month of January. Figure 6 shows the timescales at 15°S and 35°N for the following processes: chemical loss $T(\mathrm{CO})$, advection by the transformed Eulerian mean [TEM, see Andrews et al. (1987)] meridional circulation $T(v^*)$ and $T(w^*)$, and diffusive processes $T(K_{yy})$ and $T(K_{zz})$. At 15°S the photochemical lifetime is much shorter than the dynamical timescales from 10 to 1 hPa, so the upper stratosphere southern tropical CO is controlled mainly by photochemistry. At 35°N, however (Fig. 6b), the timescale for meridional diffusion $T(K_{yy})$ is comparable to the photochemical timescale $T(\mathrm{CO})$ in the upper stratosphere therefore mixing processes (largely from winter planetary wave activity) are expected to significantly affect the CO profile, as evidenced by the sharp drop off of $[CH_4]/[CO]$ northward of 10°N in Fig. 5a.

Above 2 hPa the observed $[CH_4]/[CO]$ decreases more rapidly with altitude than the predicted ratio (cf. Figs. 5a and 5b). This is likely due both to the increased dynamical contribution at higher altitudes and the increasing effect of CO_2 photolysis on the CO budget, as described below. The very large ISAMS CH_4/CO ratios observed near 10 hPa may be influenced significantly by aerosol contamination of both the CO and CH_4 ISAMS channels (López-Valverde et al. 1996; Remedios et al. 1996).

Equation (8) can be rearranged to calculate the expected CO contribution from CH_4 oxidation by OH:

$$[CO] = \frac{k_1}{k_2}[CH_4]. \tag{9}$$

The zonal-mean ISAMS CO mixing ratio (black solid line) and that calculated from Eq. (9) (dashed line) using version 12 ISAMS CH_4 are shown in Fig. 7 for 16 pressure levels on 1 January 1992. Also provided are the CO mixing ratios calculated with the GSFC 2D CTM (Jackman et al. 1996) production and loss terms for January assuming photochemical equilibrium. First we set the total CO production from the model (which includes CO_2 photolysis) equal to the loss of CO by reaction with OH ($P = k_2[\mathrm{CO}][\mathrm{OH}]$). Then we solve for [CO] using the January [OH] from the 2D model along with the rate constant k_2 from Eq. (7) and plot it with a blue line in Fig. 7. This calculation is performed again after subtracting the model's CO_2 photolysis rate from the total production. This line (red in Fig. 7) estimates the CO produced from loss of CH_4. It is close to the estimated value from Eq. (9) (dashed line), being somewhat larger (smaller) at altitudes above (below) ~2 hPa, but always remaining within a factor of 2.

In the southern tropical latitudes at 8.54 and 6.99 hPa the predicted CO mixing ratio from Eq. (9) is larger than that observed by ISAMS (cf. dashed and solid lines). From 6.99 to 1.27 hPa there is fairly good (better than 50%) agreement in magnitude between the ob-

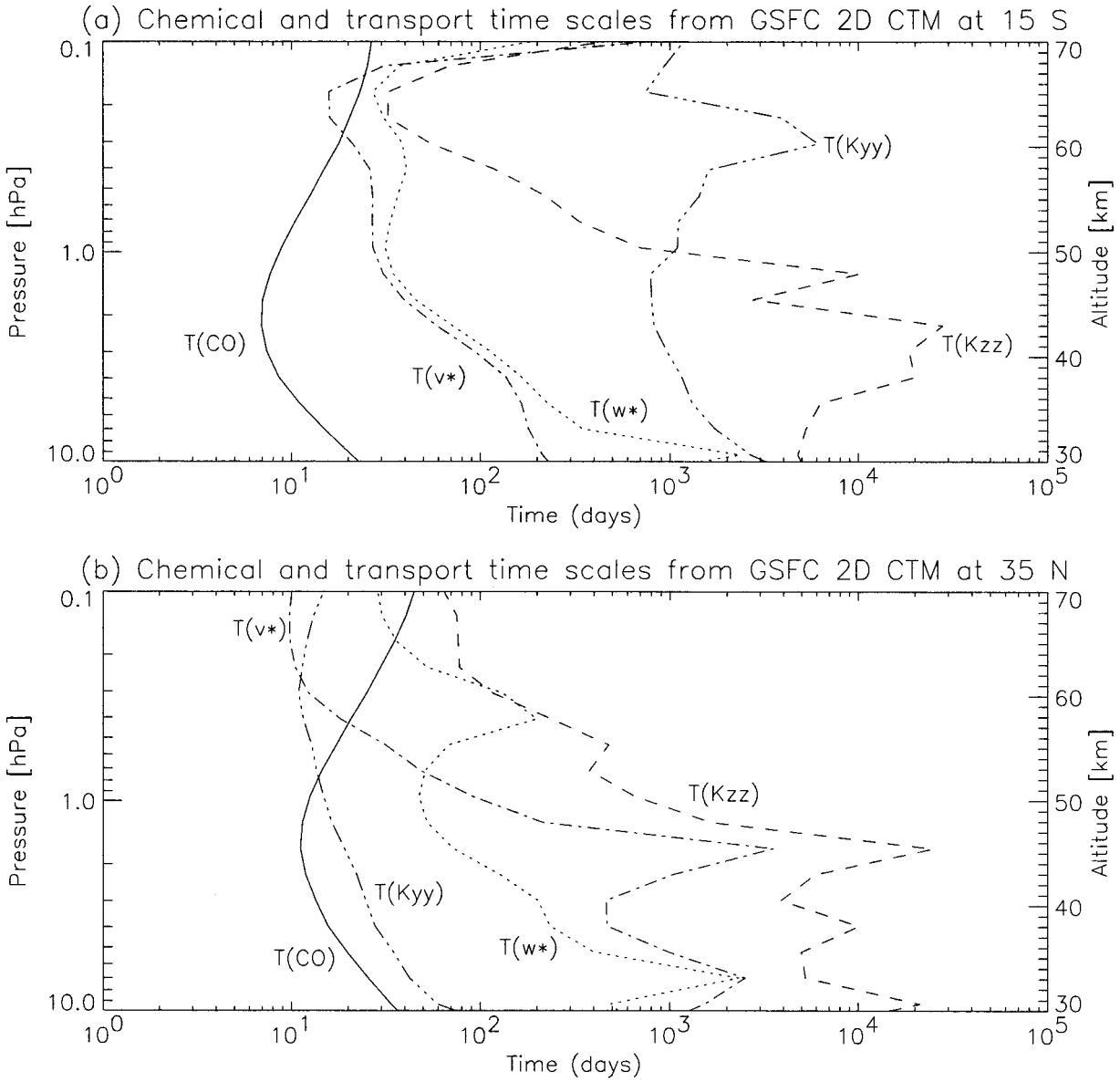

FIG. 6. Chemical and transport timescales from the GSFC 2D CTM (Jackman et al. 1996) for January at 15°S and 35°N. Timescales are for chemical loss, T(CO); advection by the transformed Eulerian mean (TEM) meridional circulation $T(v^*)$, $T(w^*)$; and diffusive processes $T(K_{yy})$, $T(K_{zz})$.

served and predicted CO from 30°S to the equator with both showing a clear maximum near 10°S from 3.77 to 1.98 hPa. A similar feature can be seen in the zonal-mean (pressure vs latitude) solstice CO distributions from the models of Solomon et al. (1985) (see their Fig. 3) and Fleming et al. (1995) (see their Fig. A-14). Both models show the low-latitude maximum in the upper stratosphere, although quantification of the strength of the maximum is difficult in each case due to widely spaced contours in the tropical stratosphere. The CO production terms from the GSFC 2D model (see Fig. 3 of this paper and the colored lines on Fig. 7) also show a low-latitude maximum, again suggesting that the feature is controlled by photochemical processes. Indeed, a passive-tracer ($P = 0$; $L = 0$) initialized in the 3D CTM with an identical distribution to ISAMS CO on 8 December 1991 shows no distinguishable tropical maximum on 1 January 1992.

At altitudes above 1.01 hPa the ISAMS CO (black line) increases rapidly with height, whereas the predicted CO from CH_4 oxidation (dashed and red lines) decreases. This is due to the increased influence of CO_2 photolysis and decreasing contribution from CH_4 oxidation. Reaction rates in Allen et al. (1981) show that above ~55 km (~0.4 hPa), the primary source of CO is from CO_2 photolysis, whereas at the stratopause (~50

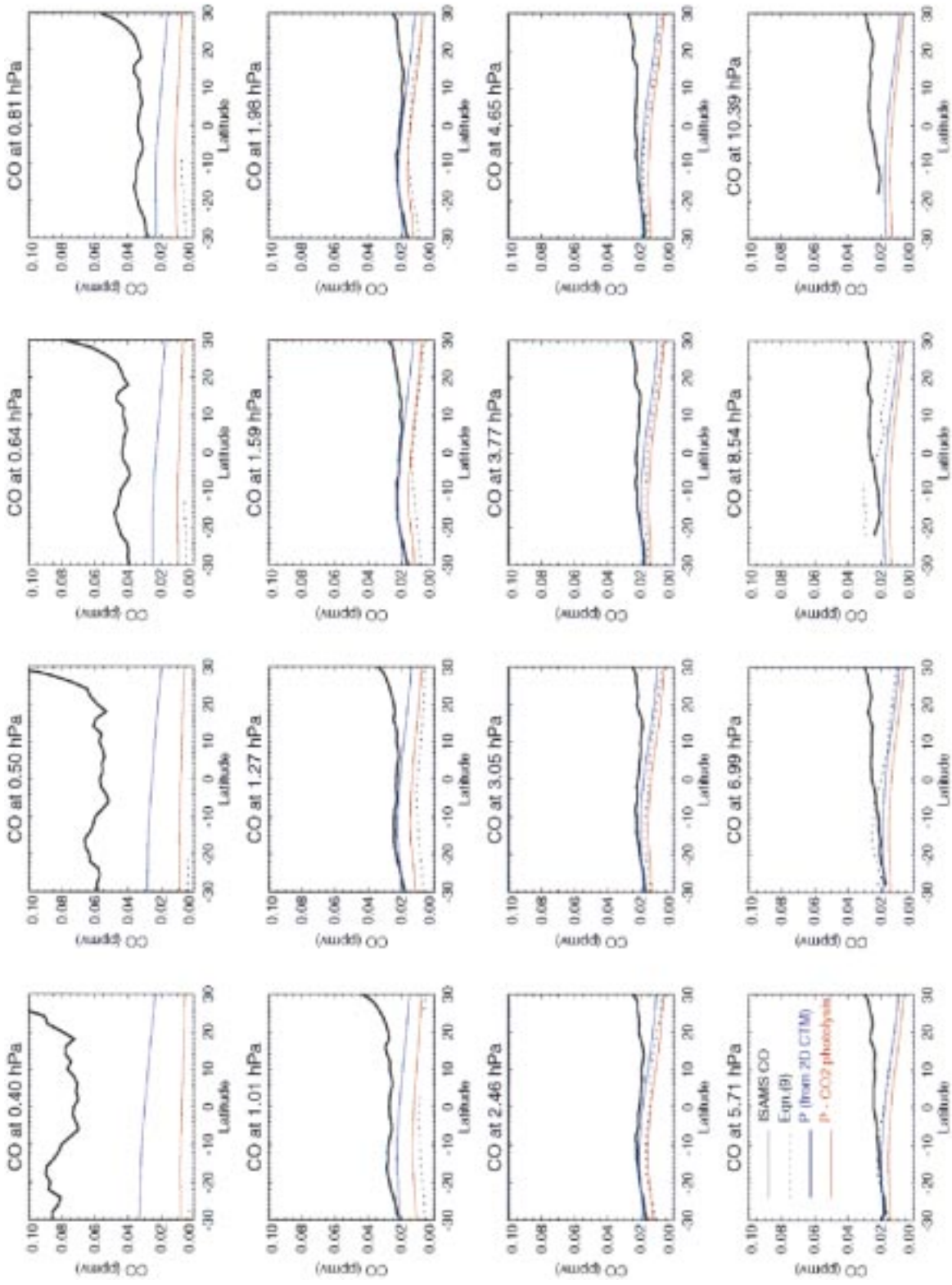

FIG. 7. Observed zonal-mean ISAMS CO (solid) and CO predicted from CH_4 oxidation [dashed, from Eq. (9)] at 16 pressure levels for 1 January 1992. Also plotted are the CO mixing ratios calculated using the GSFC 2D CTM total CO production rate (blue line) and total production minus the production from CO_2 photolysis (red line). All predictions are for daytime conditions and assume photochemical equilibrium.

km or ~1 hPa) and below, methane oxidation dominates. The CO predicted using the total CO source term from the GSFC 2D CTM (blue line) does show increased influence of CO_2 photolysis with altitude; note that the difference between the blue and red lines in Fig. 7 is due solely to CO_2 photolysis. However, above 1.01 hPa the modeled CO mixing ratio underestimates that observed by ISAMS. The difference could be caused by the increased influence of dynamical processes at higher altitudes (see Fig. 6), but it is also possible that the source term from the 2D model underestimates the CO_2 photolysis rate.

The influence of vortex excursions and/or horizontal mixing of CO-rich vortex air to low latitudes is estimated to extend to approximately 10°N from 3 to 1 hPa, where the shape of the ISAMS CO mixing ratio lines differ from the monotonically decreasing CO mixing ratio predicted from photochemical processes alone. Northward of 30°N (not shown here) the observed CO mixing ratio increases rapidly toward the pole, whereas the predicted values from CH_4 oxidation decrease monotonically.

c. Merger of two anticyclones during strong warming from 1 to 16 January 1992

The early northern winter stratosphere 1991/92 has been the subject of several observational and modeling studies. Rosier et al. (1994) examined the dynamical evolution of this period using ISAMS temperatures and derived winds and potential vorticity; O'Neill et al. (1994) used the UKMO data assimilation to study the Northern Hemisphere circulation during this winter; Ruth et al. (1994) examined tracer transport with ISAMS N_2O data; Sutton et al. (1994) applied Lagrangian trajectory calculations to study finescale mixing. We will further scrutinize this period by examining the evolution of ISAMS and CTM data in the upper stratosphere and lower mesosphere.

December 1991 to mid-January 1992 are marked by three warming events accompanied by large incursions of low-latitude air penetrating to high latitudes and tongues of polar vortex air peeling off, stretching, and mixing in low latitudes. The most significant event occurred in mid-January when an anticyclonic vortex, originating near the Greenwich Meridian, was advected eastward and merged with the persistent Aleutian high, forming an intense anticyclone that completely pushed the vortex off the pole and weakened it considerably. Here we provide a synoptic view of this vortex merger at 1 hPa (near 50 km) in ISAMS and CTM CO.

Figure 8 shows ISAMS CO at 1 hPa (colored contours) overlaid with NCEP-derived PV data at 1900 K for 1–12 January 1992, and Fig. 9 shows CTM CO (at 1 hPa) for the same period. On 1 January the vortex (identified by large values of PV and CO in Fig. 8) is centered nearly over the pole and slightly elongated on the 45°–225° long axis. A tongue of vortex air is stretched along approximately the 30°N latitude circle from 180° to 90°E. This tongue elongates farther over the next four days while a tongue of low-latitude, low-CO mixing ratio air encroaches from near 90°E (see blue region marked with arrow near 100°E, 50°N on 2 January, Fig. 8). This feature is most prominent on 3 January when the vortex exhibits a ''comma'' shape with main cell and extending tail of high PV and CO, resolved clearly by both ISAMS and the CTM. Concurrently, the Aleutian high (near 180°) is growing rapidly and by 5 January is quite strong. Both ISAMS and CTM CO on 5 January show this feature as a region of low CO mixing ratio surrounded by a ring of high CO vortex air. By this time the vortex ''tail'' has nearly reconnected with the main vortex cell near 90°E.

O'Neill et al. (1994) explain that on 6 January another anticyclone, apparent in UKMO wind fields, is beginning to form near 30°N, 30°E. This feature moves eastward (counterclockwise) over the next two days and by 8 January is centered near 70°E. The effects of this anticyclone on CO are observed by ISAMS and the CTM on 8 January as the counterclockwise winds begin to pull a tongue of CO-rich air off the main vortex near 30°N, 90°E (see arrow on Fig. 8). This tongue elongates from 9 to 11 January as the traveling anticyclone moves further eastward, advecting CO-rich air to the south, while the Aleutian high is drawn into a thin tongue. O'Neill et al. (1994) applied high resolution trajectory methods to elucidate mixing process accompanying the vortex merger. They showed that a portion of the air that constitutes the Aleutian high on 8 January was drawn into the traveling anticyclone while another portion was drawn eastward along the southern boundary of the displaced main vortex. The latter effect is clearly resolved in the CTM CO on 10 January (note the elongated region marked with arrow near 30°N, 180° to 250° long in Fig. 9), whereas ISAMS (Fig. 8) is not able to resolve the decaying Aleutian high beyond 8 January. ISAMS CO shows very good correlation with PV contours during this period; compare the vortex location and shape for 1–12 January and detached ''blobs'' of high CO and PV air on 10–12 January.

The horizontal structure on 12 January resembles that of 5 January, with a comma-shaped main vortex cell completely displaced off the pole and a strong Aleutian anticyclone surrounded by a ring of vortex air. By 12 January the vortex area has diminished significantly (compare red regions of Figs. 8 and 9 for 1 and 12 January). The trajectory analysis of O'Neill at al. (1994) revealed that the strong anticyclone on 12 January is actually composed of air that originated from three distinct vortices: the Aleutian high, the traveling anticyclone, and the polar vortex. The period from 13–16 January (not shown here) involved rapid mixing and vortex erosion that produced a highly irregular state on 16 January with nearly indistinguishable vortex (shown in Fig. 13d). A more detailed analysis of mixing processes accompanying these events is provided in section

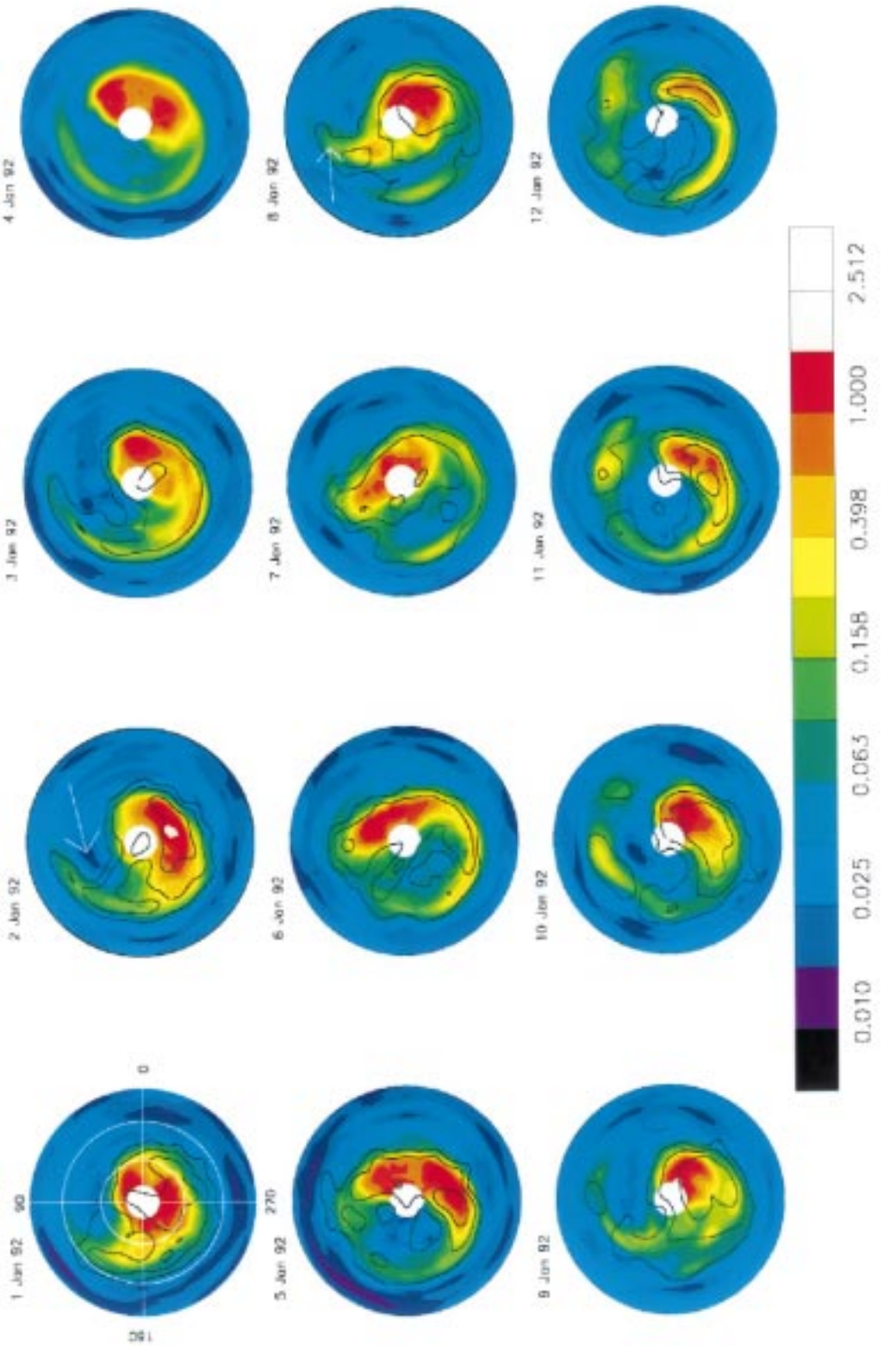

FIG. 8. Lambert equal area projections of gridded ISAMS V12 CO at 1.01 hPa for 1–12 January 1992, overlaid with contours of NCEP-derived PV at 1900 K (PV contours are at 0.006, 0.010, 0.014, 0.018, and 0.024 K m^2 kg^{-1} s^{-1}.) The grid provided on 1 January has latitude circles at 0°, 30°, and 60°N, and longitudes are indicated for every 90°. The PV data were not available on 4 January 1992.

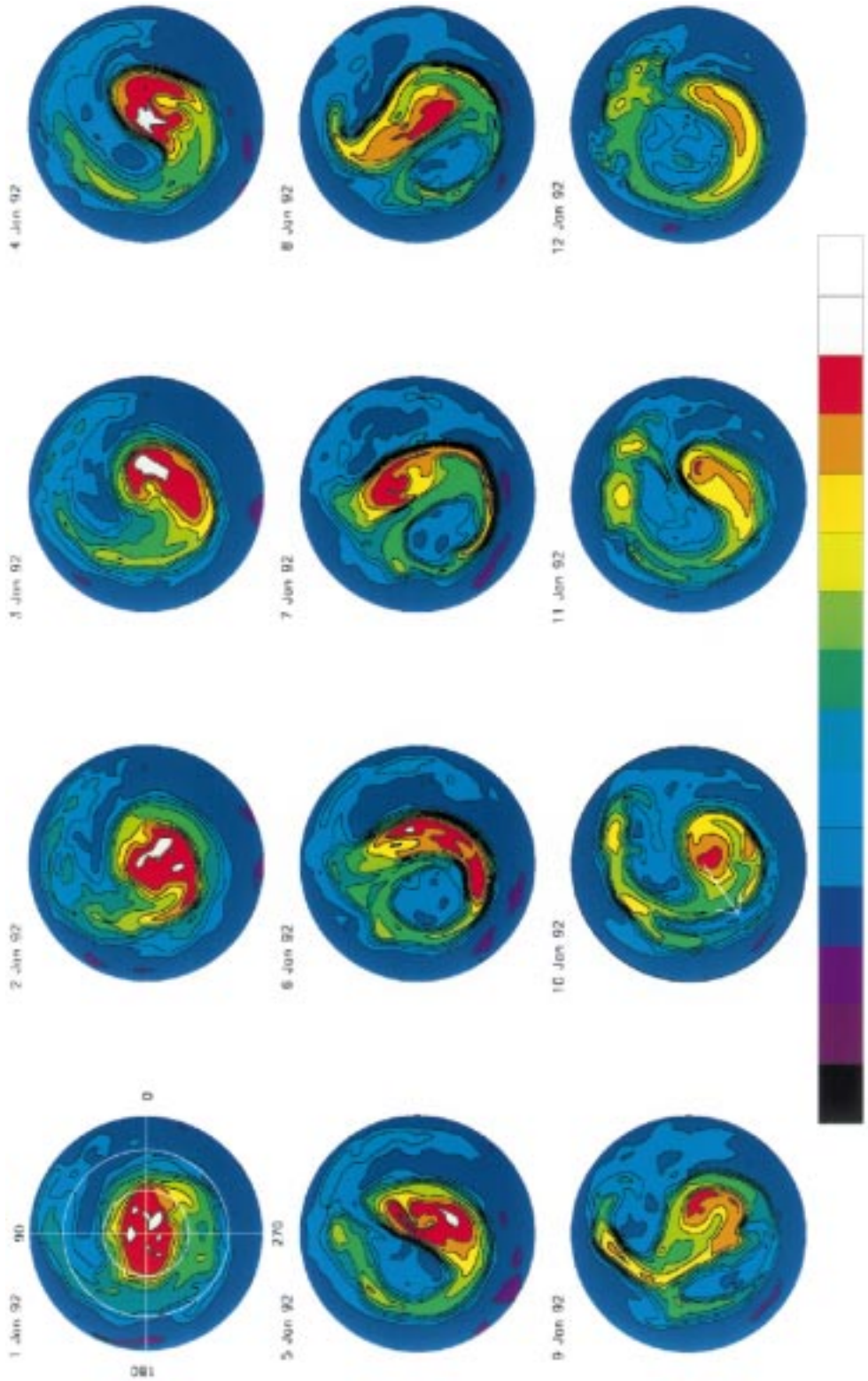

FIG. 9. Synoptic maps of GSFC 3D CTM CO at 1.01 hPa for 1–12 January 1992. Projection is identical to Fig. 8. Note: different color schemes are used for Figs. 8 and 9.

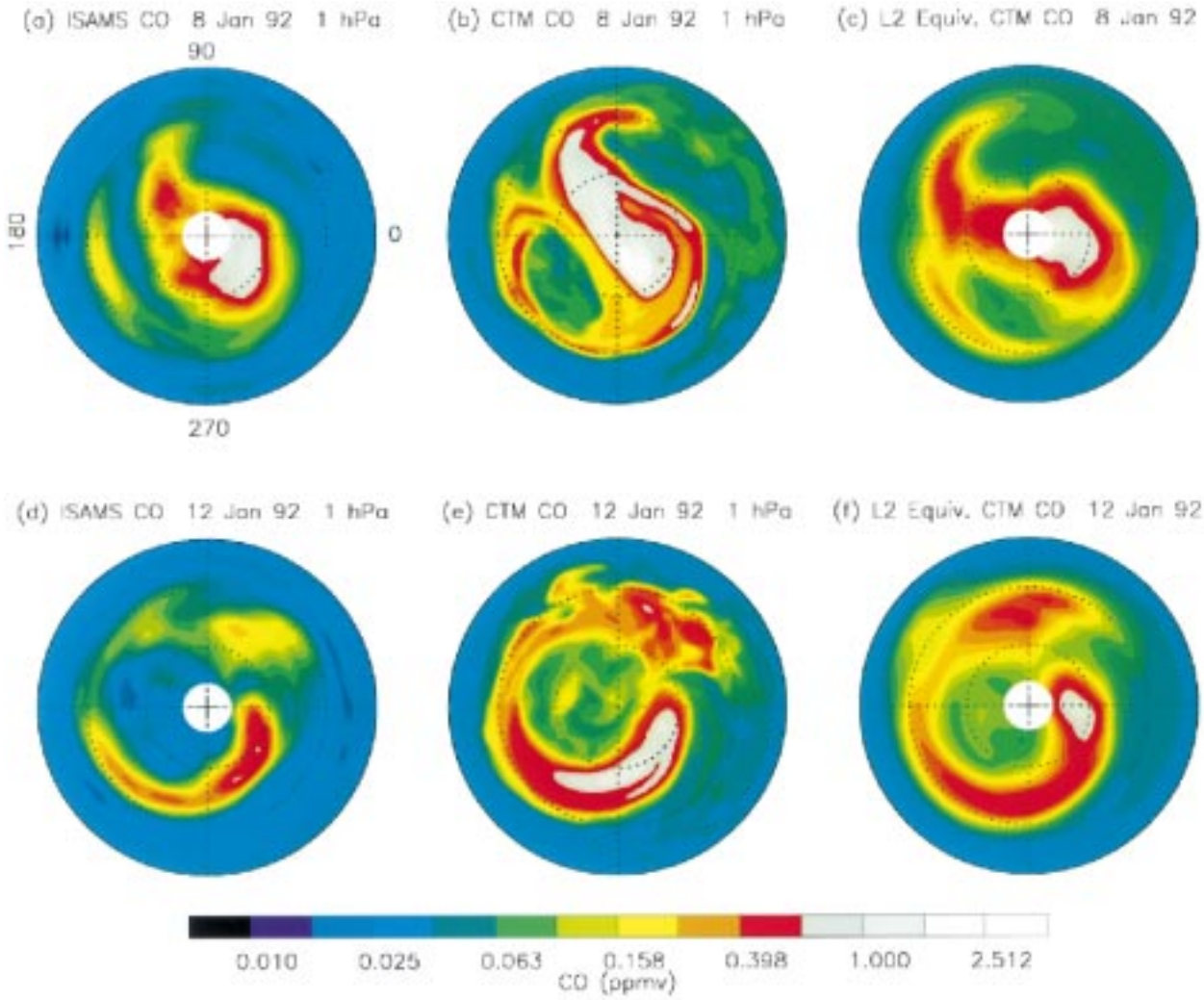

FIG. 10. (a), (d) ISAMS CO for 8, 12 January 1992 at 1 hPa. (b), (e) CTM CO for 8, 12 January at 1 hPa. (c), (f) CTM CO gridded equivalently to the ISAMS data (see text) for 8,12 January at 1 hPa. Projections are Lambert equal area with latitude circles at 0°, 30°, and 60°N.

5e, where a modified Lagrangian mean mixing diagnostic is applied to ISAMS and CTM data.

d. Comparison of ISAMS and CTM CO

A cursory comparison between ISAMS and CTM CO was made in the previous section by examining the January vortex merger at 1 hPa in ISAMS (Fig. 8) and CTM (Fig. 9) CO. A qualitative analysis of the two figures reveals the ability of both model and observations to resolve the large-scale features involved in the vortex evolution. This section compares in more detail distributions of ISAMS and CTM CO several weeks into the model run. As will be shown, the model and observations show similar horizontal morphology of the CO contours, but certain differences occur in the mean meridional distribution.

Figure 10 compares ISAMS and CTM CO for 8 and 12 January at 1 hPa along with CTM CO sampled and gridded identically to the ISAMS data (see below). On 8 January the distorted vortex with extending ''hook'' near 90°E produced from the traveling anticyclone is evident in ISAMS (Fig. 10a) and CTM (Fig. 10b) CO. The model reveals a very distinct region of low CO near 220° long associated with the strong Aleutian high, whereas in ISAMS the Aleutian high appears to be stretched into a thin tongue of low CO. This discrepancy could partly be due to the fact that whereas the CTM data are synoptic (at 0000 UTC), the ISAMS data are taken over a period of 24 h (0000–2400 UTC); as mentioned in section 2 no effort was made in the gridding of ISAMS data to correct for the asynoptic sampling.

To analyze this more closely we ''flew'' *UARS* through the CTM by linearly interpolating the synoptic CTM data in space and time to the ISAMS level 2 grid and subsequently mapped the data with the identical

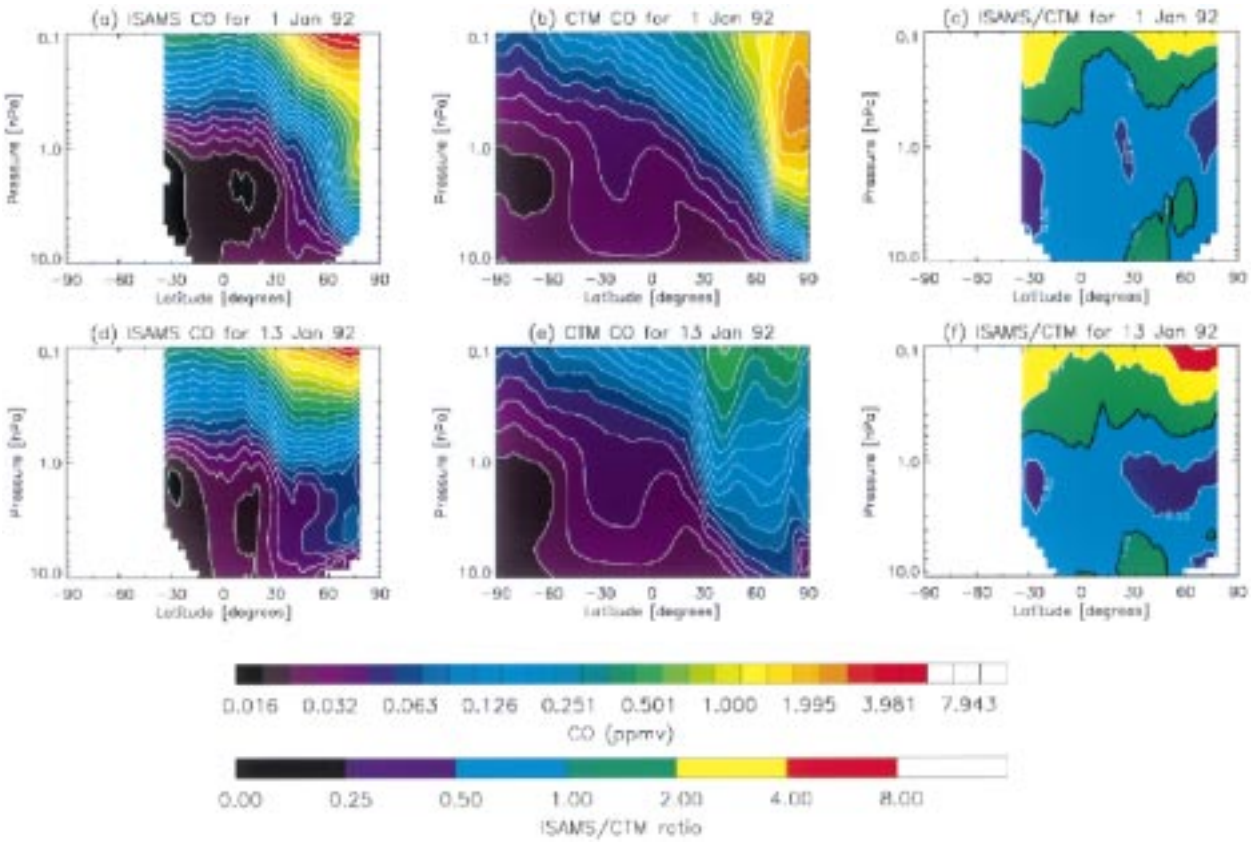

FIG. 11. Zonal-mean (a) ISAMS CO, (b) CTM CO, and (c) ISAMS/CTM ratio for 1 and January 1992. (d)–(f) Same as (a)–(c) but for 13 January 1992. The contour for ISAMS/CTM ratio of 1 is emphasized by the black line in (c) and (f).

gridding procedure used for ISAMS CO (see section 2). The resulting map for 8 January (Fig. 10c) shows a slight improvement over the synoptic CTM map in the orientation of the main vortex cell and elongated shape of the decaying Aleutian high.

On 12 January, as the vortex becomes completely displaced off the pole, both ISAMS and CTM CO show good spatial agreement of large-scale features, although the CTM CO is nearly everywhere larger than ISAMS CO. The comma-shaped vortex structure is well defined, and a region of high CO mixing ratio has been pulled from the vortex tail and has nearly reconnected with the main vortex. The model reveals finescale structure that is not resolvable by ISAMS. The ISAMS-equivalent map of CTM CO for 12 January (Fig. 10f) also shows relatively good agreement with ISAMS CO (Fig. 10d) in the shape of the polar vortex and strong Aleutian high. We conclude that both ISAMS and CTM CO capture the large-scale variability of the upper stratospheric vortex during this period.

Although the CTM is used for this study primarily to examine the horizontal distributions of CO, we also present a zonal-mean comparison in the meridional plane as an example of how ISAMS CO can be used to diagnose model deficiencies and vice versa. Zonal-mean plots of ISAMS and CTM CO from 10 to 0.1 hPa on 1 and 13 January 1992 (24 and 36 days after initialization) are provided in Fig. 11 along with the ISAMS/CTM ratio. On 1 January both ISAMS and CTM CO show strong meridional gradients near 60°N from 5 to 1.0 hPa, signifying the ''edge'' of the polar vortex. The low-latitude double-lobed minima in the upper stratosphere are evident in ISAMS at 30°S and 15°N (see Fig. 11a); minima are also present in the CTM near 60°S and 15°N (see Fig. 11b), but are not as distinct. By 13 January this feature becomes more obscured in the model as a broad upper-stratospheric maximum sets in from 60°S to 15°N (Fig. 11e), whereas ISAMS continues to display a compact double-lobed structure (Fig. 11d).

Vertical gradients in ISAMS tend to be larger than in the model from 1 to 0.1 hPa on both 1 and 13 January. The ISAMS/CTM ratios provided in Fig. 11c,f show that the ISAMS CO mixing ratios are larger than the CTM CO by about a factor of 2–3 near 0.1 hPa and smaller throughout most of the upper stratosphere (10–1.0 hPa). The contour of ISAMS/CTM = 1 is highlighted in black. On 13 January both ISAMS and CTM show strong horizontal gradients near 30°N and weak horizontal gradients poleward of 30°N above ~1 hPa.

The weakening of the horizontal gradients from 1 to 13 January is due to the polar vortex breakdown accompanied by large horizontal mixing discussed in sections 5c and 5e.

The weaker vertical gradients observed in the CTM are likely due to several competing factors. Notably, there are some questionable features in the residual circulation used in this study. Zonal-mean latitude–height cross sections of CTM CO (not shown here) show an unexpected decrease in CO in the Northern Hemisphere high latitudes above ~1 hPa throughout the run. This is due to unrealistic upward motion in the model, which dilutes CO mixing ratios. In this region the photochemical lifetime is very long (see Fig. 3f) so discrepancies are expected to be due to errors in transport rather than chemistry. In the Tropics, however, the photochemical lifetime is comparable to or smaller than the dynamical timescales (see Fig. 6a) so discrepancies there could be influenced by errors in the model photochemistry. The analysis presented in section 5b, for example, suggests that the CTM may be underestimating the CO production from CO_2 photolysis at higher altitudes. Further limitations of the model that could factor into the discrepancy with observations include the upper boundary constraint of zero vertical velocity at 0.01 hPa, which does not allow downward flux of CO from the upper mesosphere and the exclusion of explicit horizontal and vertical subgrid-scale diffusion. A complete diagnosis of the relative contribution from each of these factors is planned for future work.

Although further examination of ISAMS version 12 CO is necessary, the comparison of ISAMS CO with PV and CTM CO presented here provides a useful preliminary validation of ISAMS data quality as well as constraints on the CTM, which may help to improve the model's transport and chemistry in the upper stratosphere and lower mesosphere. The good agreement in horizontal morphology lends confidence to the use of ISAMS CO as a tracer to identify rapidly varying zonally asymmetric features in the upper stratosphere/lower mesosphere and provides validation for the horizontal winds and transport scheme used by the CTM. The discrepancies in the mean meridional structure points to possible model deficiencies and provides incentive for a more thorough validation of ISAMS and CTM CO.

e. MLM diagnostics of vortex merger

The equivalent length (L_e) described in section 4 can be used to examine barrier evolution and mixing that accompany large stratospheric wave events. Here L_e provides both a diagnostic for the instantaneous degree of scrambling of the tracer isopleths as well as the ''effective horizontal diffusivity,'' which drives the tracer distribution in the MLM coordinates. Local minima in L_e generally indicate barriers to horizontal mixing, whereas maxima indicate regions where large mixing is expected (see Nakamura 1996, 1998). Figure 12 provides synoptic maps of ISAMS CO at 1 hPa for 1 and 6 January 1992 along with normalized equivalent length, $\xi = \ln(L_e^2/L_o^2)$, where $L_o = 2\pi a \cos\phi_e$ is the circumference of the zonal circle at latitude ϕ_e, the equivalent latitude defined by $A(\chi, t) = 2\pi a^2(1 - \sin\phi_e)$, where a is the earth's radius. On 1 January the circumpolar vortex is slightly elongated on the 45°–225° axis with an emerging tail and intruding tongue of low-latitude air; ξ for this tracer distribution (Fig. 12b) displays a minimum near 60° equivalent latitude, indicating a mixing barrier. The location of the 60° equivalent latitude contour, identified by black contour on Fig. 12a, shows that the mixing barrier is near the vortex ''edge,'' identified here by strong CO gradients. Five days later the vortex has been pushed off the pole and is deformed into a ''comma'' shape. Here ξ no longer shows a local minimum near 60° indicating that the distinct mixing barrier has weakened considerably; the situation on 6 January is more likely to experience horizontal mixing across the 60° contour. As explained in section 4, L_e also gives to a good approximation of the perimeter length of a given contour. As evident from Fig. 12 the length of the 60° equivalent latitude contour has increased from 1 to 6 January.

To examine the meridional structure of mixing processes during January 1992, MLM diagnostics are applied to CTM output from 10 to 0.1 hPa. MLM assumes mixing ratios are generally monotonically increasing or decreasing with latitude in the region of interest. Due to the tropical upper stratosphere maximum in CO, MLM cannot be reliably applied to CO in that region. However, if two tracers are in contour equilibrium (i.e., their contours overlap, even if the gradients differ) one can prove mathematically (see appendix) that their equivalent lengths will be identical. A comparison of CTM CO (Figs. 13a–d) with CTM N_2O (Figs. 13e–h) for 1, 6, 11, and 16 January shows that CO and N_2O at 1 hPa have similar contour shapes. Since N_2O has monotonic gradients throughout the Northern Hemisphere stratosphere, we can apply MLM diagnostics to N_2O as a surrogate for CO to obtain a 2D picture of barrier evolution and horizontal mixing.

The normalized equivalent length ξ at 1 hPa on 1 January 1992 calculated from CTM N_2O is provided in Fig. 14e. This shows similar structure to ξ calculated from ISAMS CO (Fig. 12b), although the mixing barrier appears relatively stronger and is centered near 70° rather than 60° equivalent latitude. The difference in magnitude of ξ between the ISAMS and CTM analyses is due partly to the different horizontal resolution of the two datasets [see Nakamura and Ma (1997) for discussion of resolution dependence]. Figures 14a–d show the N_2O mixing ratio as a function of equivalent latitude at 1 hPa. The minimum in ξ on 1 January is colocated with a strong gradient of N_2O with equivalent latitude near the vortex edge. The mixing barrier appears to weaken by 6 January as ξ near 70° equivalent latitude increases to midlatitude levels (similar to Fig. 12d); it

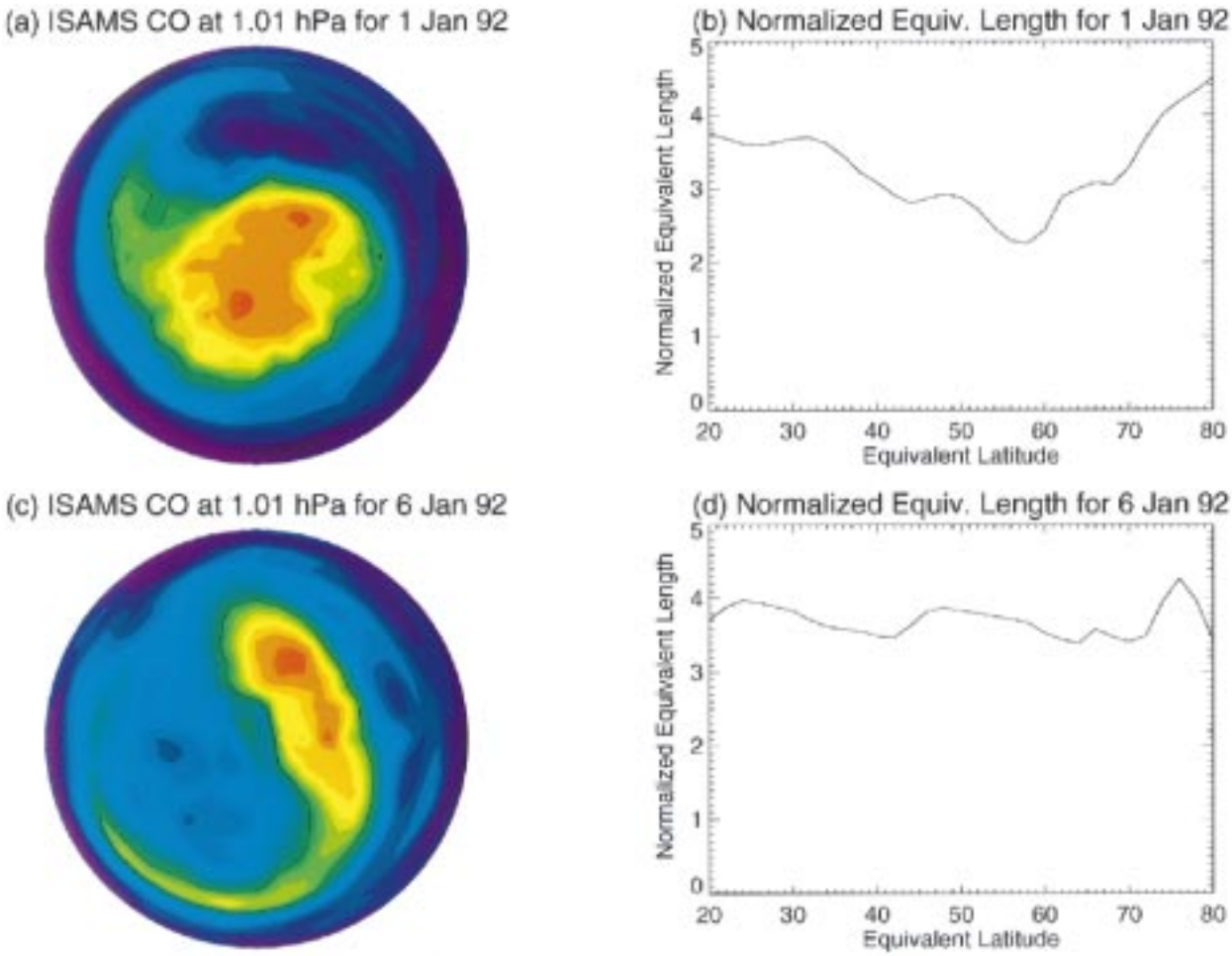

FIG. 12. (a) ISAMS CO and (b) normalized equivalent length ξ (from the MLM formulation, see text) at 1.01 hPa for 1 January 1992. (c), (d) Same as (a), (b) but for 6 January 1992. Projection for (a), (c) is identical to Fig. 8.

attempts a slight comeback by 11 January, but is completely eliminated by 16 January, when a broad region of large ξ develops from 40° to 70° equivalent latitude. The rapid mixing occurring during this period is evident in the synoptic plots of CTM CO (Figs. 13a–d) and CTM N_2O (Figs. 13e–h). The main vortex cell, highlighted in Fig. 13 by white/gray regions in CO and deep blue/purple regions in N_2O, which covers a large area on 1 January, has nearly disappeared by 16 January, leaving a broad well-mixed region in the upper stratosphere. Interestingly, although ξ responds rapidly to tracer contour deformation the tracer-area (or tracer-ϕ_e) relation shown in Figs. 14a–d does not change significantly over this time period. As expected from the definition of L_e in Eq. (5) there is a tendency for the magnitude of the slope of the tracer-area curve $|\partial\chi/\partial A|$ to be smaller in magnitude when L_e is large; see, for example, the broad region of relatively weak slope in Fig. 14d from 40° to 70° equivalent latitude where ξ is large (Fig. 14h). Also note that the steep slope observed on 1 January (Fig. 14a) weakens with the decay of the mixing barrier.

Maps of ξ are plotted in Figs. 14i–l as a function of pressure and equivalent latitude. On 1 January a strong barrier is evident at 70° from 10 to 1 hPa with minimal regions of large mixing (here defined arbitrarily by $\xi \geq 2.8$, i.e., $L_e \sim 4L_o$). Five days later (Fig. 14j) the barrier has weakened significantly while a region of large ξ develops roughly from 20° to 45° equivalent latitude and 1 to 0.1 hPa. The polar upper-stratospheric barrier strengthens slightly by 11 January (Fig. 14k) while the entire lower mesosphere becomes saturated by large equivalent lengths. By 16 January the lower mesosphere is thoroughly mixed as values of ξ greater than 2.8 extend from 20° to 80° equivalent latitude, and the upper stratosphere shows a broad well-mixed ''surf zone'' region from 50° to 60° near 10 hPa, widening to 40° to 70° near 1 hPa.

These analyses indicate that the well-mixed region from 1 to 16 January first appears in the mesosphere

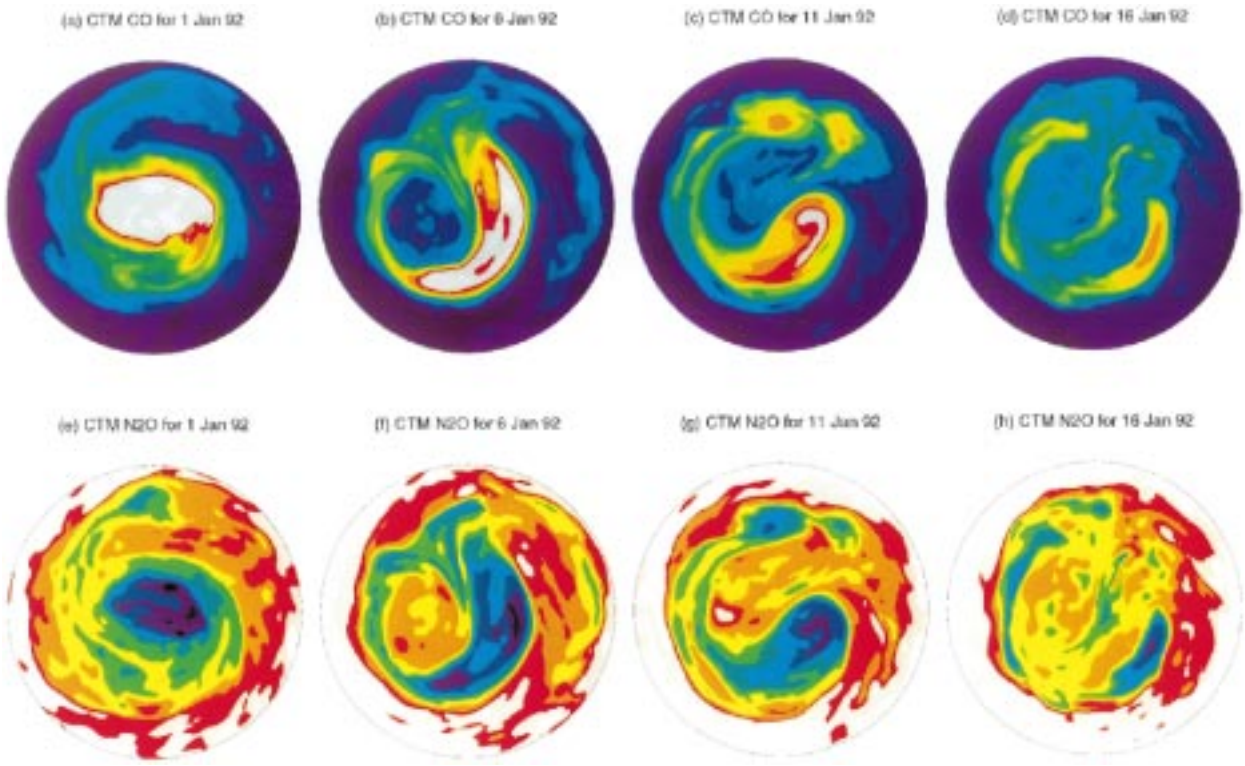

FIG. 13. (a)–(d) CTM CO at 1 hPa for 1, 6, 11, and 16 January 1992 with same projection as Figs. 12a,c. (e)–(h) CTM N_2O at 1 hPa. White (purple) indicates large (small) mixing ratio.

and subsequently descends through the upper stratosphere. This descent is consistent with the general theory of stratospheric sudden warming first proposed by Matsuno (1971) in which vertically propagating, tropospherically forced planetary waves act to decelerate (or ''break down'') the westerly polar night vortex. The wave amplitudes increase with altitude (due to the decrease in air density) until they reach a critical layer where the phase speed equals the zonal wind speed. Near the critical layer the wave ''breaks,'' causing an easterly acceleration that weakens the westerly jet. The altitude of the critical layer then decreases with time as the westerly jet turns easterly, so planetary waves break at progressively lower altitude, consistent with the time evolution of the L_e diagnostic displayed in Figs. 12i–l.

6. Summary and conclusions

This paper presents observations of ISAMS CO from 10 to 0.03 hPa during the dynamically active early northern winter 1991/92. The mean meridional structure agrees with previous 2D model predictions; CO mixing ratio generally increases with height in the upper stratosphere and lower mesosphere and increases with latitude toward the winter pole. A previously unreported maximum in CO mixing ratio occurs in the tropical upper stratosphere. This feature is attributed largely to the CO source from methane destruction.

Large CO mixing ratios are found in the winter polar vortex due to diabatic descent and long photochemical lifetime. Because of the latter, CO is a useful tracer of polar vortex dynamics. In January 1992, the merger of the upper-stratospheric Aleutian high with a traveling anticyclone is well captured by the synoptic evolution of ISAMS CO data. Carbon monoxide becomes a particularly important tracer near the stratopause and above, where the detection of many long-lived tracers becomes difficult due to their decreasing mixing ratios with altitude.

The evolution of ISAMS CO is compared with output from a 6-week run of the GSFC 3D CTM. The synoptic evolutions of ISAMS and CTM CO compare well at 1 hPa during the highly dynamic period from 1 to 12 January 1992, whereas two obvious differences are evident in the zonal-mean meridional distributions from 10 to 0.1 hPa. First, a relative weakening in the model vertical gradients occurs compared with ISAMS. Second, the model is not able to capture the persistent tropical upper-stratospheric maximum observed in ISAMS.

Modified Lagrangian mean diagnostics are applied to ISAMS CO and CTM N_2O to examine the evolution of mixing barriers in early January 1992. Mixing barriers and regions of significant mixing are identified by minima and maxima in the constituent ''equivalent length,'' a modified Lagrangian mean diagnostic. This diagnostic, unlike time-averaged ''eddy diffusivity'' parameters

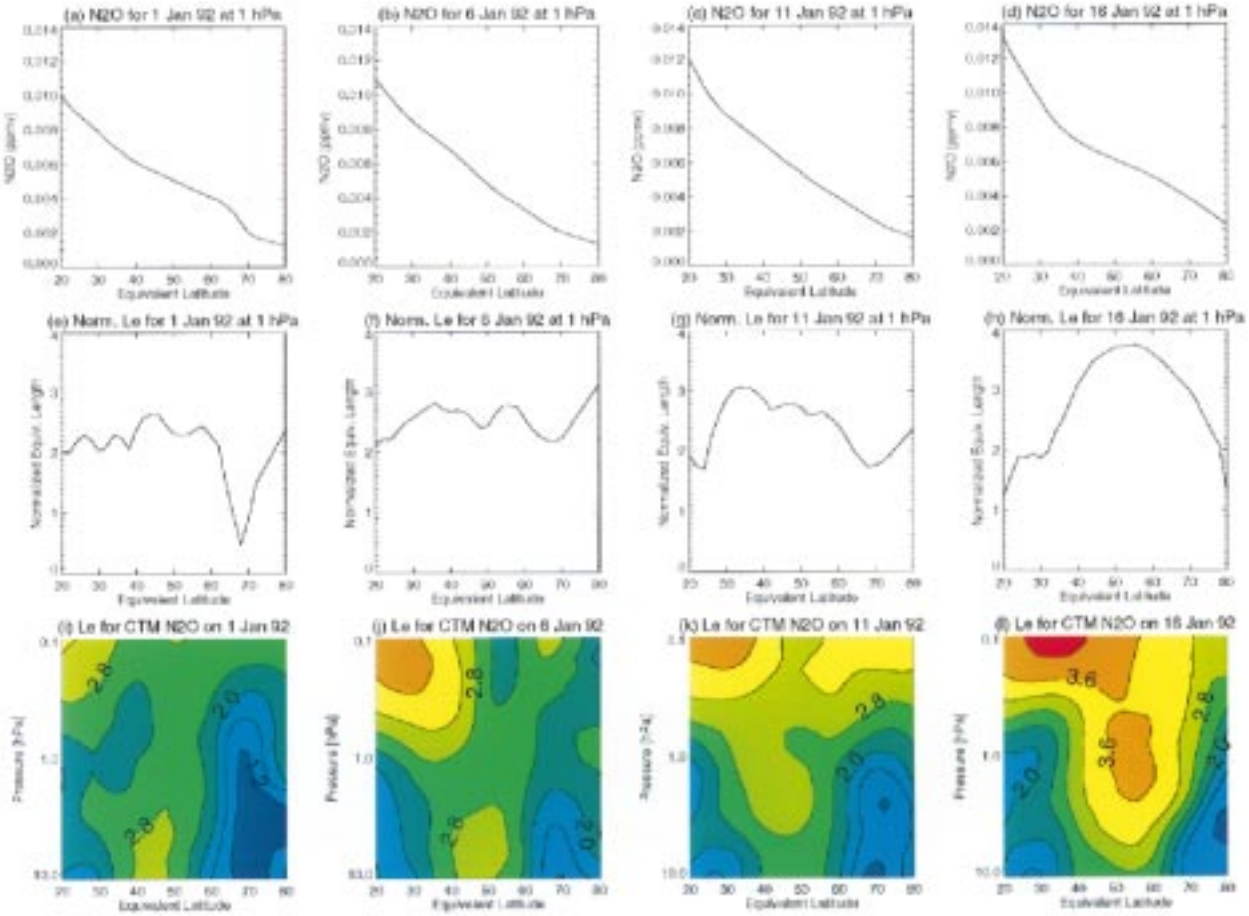

FIG. 14 (a)–(d) CTM N_2O as function of equivalent latitude at 1 hPa for 1, 6, 11, and 16 January 1992. (e)–(h) Normalized equivalent length ξ calculated from CTM N_2O at 1 hPa. (i)–(l) Two-dimensional cross section of normalized equivalent length calculated from CTM N_2O. Contour interval is 0.4.

common among two-dimensional models, is defined instantaneously; as a result, it is better suited to describe the process of a mixing event (Nakamura 1996). For 1 January 1992 a mixing barrier is identified near the vortex edge in both ISAMS CO and CTM N_2O. This barrier weakens over the next two weeks as planetary wave activity erodes the polar vortex, leaving a well-mixed lower mesosphere and broad ''surf zone'' in the upper stratosphere. The altitude of strong polar vortex erosion, as viewed in the MLM framework, appears to descend from mesosphere into the upper stratosphere. This is consistent with the idea that vortex dissipation is caused by the breaking of vertically propagating planetary waves.

In conclusion, we have demonstrated that, used with care, ISAMS CO data can enhance our understanding of the dynamics and chemistry of the upper stratosphere and lower mesosphere. The data are useful for both observations and model comparisons.

Acknowledgments. We want to thank three anonymous reviewers for helpful comments on the manuscript and R. J. Wells for invaluable assistance with the ISAMS data. R. Swinbank and A. O'Neill developed the UKMO data (used in the PV-mapping) from which PV was calculated using code from M. Chipperfield. A. Miller and M. Gelman developed the NCEP data from which PV was derived and provided to us by G. Manney. Many of the IDL and FORTRAN programs used for this study were modified from programs written by H. Pumphrey. We also want to thank R. Rood, K. Ekers, and the entire GSFC (DAO, code 915) Data Assimilation Office for providing winds from the ''PREFGGEO'' assimilation that were used in this study. *UARS* level 3AT data were obtained from the Earth Observing System (EOS) Distributed Active Archive Center (DAAC, code 902.2) at the GSFC, Greenbelt, MD. The activities of the EOS DAAC and the *UARS* Project (code 916) are sponsored by NASA's Mission to Planet Earth Program. ISU coauthors are sponsored in part by National Aeronautics and Space Administration Grant NAG 5-2787. Part of this work was done while D. Allen was a Guest Graduate Student at Argonne National Laboratory, Argonne, IL.

APPENDIX

Proof that Equivalent Length is the Same for all Species in Contour Equilibrium

By definition any two tracers in contour equilibrium hold a compact relationship. That is, the mixing ratio of one is specified by that of another:

$$\chi_1(x, y, \theta, t) = \chi_1(\chi_2(x, y, \theta, t)), \tag{A1}$$

where χ_1 and χ_2 are the mixing ratios of the two species. The above relationship does not necessarily have to be monotonic (one-to-one). Equivalent length defined through χ_1 is

$$L_e^2 = (\partial\chi_1/\partial A)^{-2}\langle|\nabla\chi_1|^2\rangle, \tag{A2}$$

where the angle brackets denote the contour average. However, since

$$\frac{\partial\chi_1}{\partial A} = \frac{d\chi_1}{d\chi_2}\frac{\partial\chi_2}{\partial A}; \qquad \nabla\chi_1 = \frac{d\chi_1}{d\chi_2}\nabla\chi_2, \tag{A3}$$

Eq. (A3) can be rewritten as

$$L_e^2 = (\partial\chi_1/\partial A)^{-2}\langle|\nabla\chi_1|^2\rangle$$

$$= (\partial\chi_2/\partial A)^{-2}(d\chi_1/d\chi_2)^{-2}\langle(d\chi_1/d\chi_2)^2|\nabla\chi_2|^2\rangle \tag{A4}$$

$$= (\partial\chi_2/\partial A)^{-2}\langle|\nabla\chi_2|^2\rangle. \tag{A5}$$

The last identity uses the fact that $d\chi_1/d\chi_2$ is a constant on the tracer contour. Hence equivalent length is identical whether χ_1 or χ_2 is used. Notice, however, that the gradients of the two tracers are not necessarily the same since in general $d\chi_1/d\chi_2 \neq 1$ in Eq. (A3).

REFERENCES

Aellig, C. P., N. Kämpfer, and A. Hauchecorne, 1995: Variability of mesospheric CO in the fall and winter as observed with ground-based microwave radiometry at 115 GHz. *J. Geophys. Res.*, **100,** 14 125–14 130.

Allen, M., Y. Yung, and J. W. Waters, 1981: Vertical transport and photochemistry in the terrestrial mesosphere and lower thermosphere (50–120 km). *J. Geophys. Res.*, **86,** 3617–3627.

Andrews, D. G., J. R. Holton, and C. B. Leovy, 1987: *Middle Atmosphere Dynamics.* Academic Press, 489 pp.

Bevilacqua, R. M., A. A. Stark, and P. R. Schwartz, 1985: The variability of carbon monoxide in the terrestrial mesosphere as determined from ground-based observations of the J = 1 → 0 emission line. *J. Geophys. Res.*, **90,** 5777–5782.

Brasseur, G., and S. Solomon, 1986: *Aeronomy of the Middle Atmosphere.* 2d ed. D. Reidel, 452 pp.

Chang, A. Y., and Coauthors, 1996: A comparison of measurements from ATMOS and instruments aboard the ER-2 aircraft: Tracers of atmospheric transport. *Geophys. Res. Lett.*, **23,** 2389–2392.

Clancy, R. T., D. O. Muhleman, and G. L. Berge, 1982: Microwave spectra of terrestrial mesospheric CO. *J. Geophys. Res.*, **87,** 5009–5014.

——, ——, and M. Allen, 1984: Seasonal variability of CO in the terrestrial mesosphere. *J. Geophys. Res.*, **89,** 9673–9676.

DAO, 1996: Algorithm theoretical basis document. Data Assimilation Office, NASA/Goddard Space Flight Center, Greenbelt, MD. [Available online at http://dao.gsfc.nasa.gov/.]

DeMore, W. B., and Coauthors, 1997: Chemical kinetics and photochemical data for use in stratospheric modeling. JPL Pub. 97-4, 266 pp. [Available from Jet Propulsion Laboratory, California Institute of Technology, Document Distribution, MS S12-110, 4800 Oak Grove Drive, Pasadena, CA 91109.]

Douglass, A. R., C. J. Weaver, R. B. Rood, and L. Coy, 1996: A three-dimensional simulation of the ozone annual cycle using winds from a data assimilation system. *J. Geophys. Res.*, **101,** 1463–1474.

Fleming, E. L., S. Chandra, C. H. Jackman, D. B. Considine, and A. R. Douglass, 1995: The middle atmospheric response to short and long term solar UV variations: Analysis of observations and 2D model results. *J. Atmos. Terr. Phys.*, **57,** 333–365.

Girard, A., and Coauthors, 1988: Global results of grill spectrometer experiment on board Spacelab 1. *Planet. Space Sci.*, **36,** 291–300.

Goldsmith, P. F., M. M. Litvak, R. L. Plambeck, and D. R. Williams, 1979: Carbon monoxide mixing ratios in the mesosphere derived from ground-based microwave measurements. *J. Geophys. Res.*, **84,** 416–418.

Gunson, M. R., and Coauthors, 1996: The atmospheric trace molecule spectroscopy (ATMOS) experiment: Deployment on the ATLAS space shuttle missions. *Geophys. Res. Lett.*, **23,** 2333–2336.

——, C. B. Farmer, R. H. Norton, R. Zander, C. P. Rinsland, J. H. Shaw, and B.-C. Gao, 1990: Measurements of CH_4, N_2O, CO, and O_3 in the middle atmosphere by the atmospheric trace molecule spectroscopy experiment on Spacelab 3. *J. Geophys. Res.*, **95,** 13 867–13 882.

Hays, P. B., and J. J. Olivero, 1970: Carbon dioxide and monoxide above the tropopause. *Planet. Space Sci.*, **18,** 1729–1733.

Jackman, C. H., E. L. Fleming, S. Chandra, D. B. Considine, and J. E. Rosenfield, 1996: Past, present, and future modeled ozone trends with comparisons to observed trends. *J. Geophys. Res.*, **101,** 28 753–28 767.

Kunzi, K. F., and E. R. Carlson, 1982: Atmospheric CO volume mixing ratio profiles determined from ground-based measurements of the J = 1 → 0 and J = 2 → 1 emission lines. *J. Geophys. Res.*, **87,** 7235–7241.

Lary, D., M. P. Chipperfield, J. A. Pyle, W. A. Norton, and L. P. Riishojgaard, 1995: Three-dimensional tracer initialization and general diagnostics using equivalent latitude-potential-temperature coordinates. *Quart. J. Roy. Meteor. Soc.*, **121,** 187–210.

Lin, S. J., and R. B. Rood, 1996: Multidimensional flux form semi-Lagrangian transport schemes. *Mon. Wea. Rev.*, **124,** 2046–2070.

López-Puertas, M., M. A. López-Valverde, D. P. Edwards, and F. W. Taylor, 1993: Non-local thermodynamic equilibrium populations of the first vibrational excited state of CO in the middle atmosphere. *J. Geophys. Res.*, **98,** 8933–8947.

López-Valverde, M. A., M. López-Puertas, and C. J. Marks, 1991: Non-LTE modelling for the retrieval of CO abundances from ISAMS measurements. *Tech. Dig. Opt. Rem. Sens. Atmos.*, **18,** 31–33.

——, ——, ——, and F. W. Taylor, 1993: Global and seasonal variations in the middle atmosphere carbon monoxide from UARS/ISAMS. *Geophys. Res. Lett.*, **20,** 1275–1278.

——, ——, J. J. Remedios, C. D. Rodgers, F. W. Taylor, E. C. Zipf, and P. W. Erdman, 1996: Validation of measurements of carbon monoxide from the improved stratospheric and mesospheric sounder. *J. Geophys. Res.*, **101,** 9929–9955.

——, ——, F. W. Taylor, and M. Gunson, 1998: Correlations between ISAMS and ATMOS measurements of CO in the middle atmosphere. *Adv. Space Res.*, in press.

Matsuno, T., 1971: A dynamical model of the stratospheric sudden warming. *J. Atmos. Sci.*, **28,** 1479–1494.

McIntyre, M. E., 1980: Towards a Lagrangian-mean description of stratospheric circulations and chemical transport. *Philos. Trans. Roy. Soc. London*, **A296,** 129–148.

Murphy, A. K., 1985: Satellite measurements of atmospheric trace gases. Ph. D. thesis, Oxford University, 232 pp. [Available from Atmospheric, Oceanic, and Planetary Physics Library, Clarendon Laboratory, Parks Road, Oxford OX1 3PU, United Kingdom.]

Nakamura, N., 1995: Modified Lagrangian-mean diagnostics of the stratospheric polar vortices. Part I: Formulation and analysis of GFDL SKYHI GCM. *J. Atmos. Sci.,* **52,** 2096–2108.

——, 1996: Two-dimensional mixing, edge formation, and permeability diagnosed in an area coordinate. *J. Atmos. Sci.,* **53,** 1524–1537.

——, 1998: Leaky containment vessels of air: A Lagrangian-mean approach to the stratospheric tracer transport. *Advances in Fluid Mechanics Series: Dynamics of Atmospheric Flows. Part I. Atmospheric Transport and Diffusion Processes,* M. P. Singh and S. Raman, Eds, Computational Mechanics Publications, 193–246.

——, and J. Ma, 1997: Modified Lagrangian-mean diagnostics of the stratospheric polar vortices. Part II: Nitrous oxide and seasonal barrier migration in the cryogenic limb array etalon spectrometer and SKYHI general circulation model. *J. Geophys. Res.,* **102,** 25 721–25 735.

O'Neill, A., W. M. Grose, V. D. Pope, H. Maclean, and R. Swinbank, 1994: Evolution of the stratosphere during the northern winter 1991/92 as diagnosed from U.K. Meteorological Office analyses. *J. Atmos. Sci.,* **51,** 2800–2817.

Remedios, J. J., and Coauthors, 1996: Measurements of methane and nitrous oxide distributions by the improved stratospheric and mesospheric sounder: Retrieval and validation. *J. Geophys. Res.,* **101,** 9843–9871.

Rinsland, C. P., M. R. Gunson, R. Zander, and M. López-Puertas, 1992: Middle and upper atmosphere pressure–temperature profiles and the abundances of CO_2 and CO in the upper atmosphere from ATMOS/Spacelab 3 observations. *J. Geophys. Res.,* **97,** 20 479–20 495.

Rosier, S. M., B. N. Lawrence, D. G. Andrews, and F. W. Taylor, 1994: Dynamical evolution of the northern stratosphere in the early winter 1991/92, as observed by the improved stratospheric and mesospheric sounder. *J. Atmos. Sci.,* **51,** 2783–2799.

Ruth, S. L., J. J. Remedios, B. N. Lawrence, and F. W. Taylor, 1994: Measurements of N_2O by the UARS improved stratospheric and mesospheric sounder during the early northern winter 1991/92. *J. Atmos. Sci.,* **51,** 2818–2833.

Schoeberl, M. R., and Coauthors, 1989: Reconstruction of the constituent distribution and trends in the Antarctic polar vortex from ER-2 flight observations. *J. Geophys. Res.,* **94,** 16 815–16 845.

——, and L. R. Lait, 1991: Conservative coordinate transformations for atmospheric measurements. *EOS NATO Summer School,* G. Visconti and J. Gille, Eds., American Geophysical Union, 419–431.

Schubert, S. D., R. B. Rood, and J. Pfaendtner, 1993: An assimilated data set for earth science applications. *Bull. Amer. Meteor. Soc.,* **74,** 2331–2342.

Solomon, S., R. R. Garcia, J. J. Olivero, R. M. Bevilacqua, P. R. Schwartz, R. T. Clancy, and D. O. Muhleman, 1985: Photochemistry and transport of carbon monoxide in the middle atmosphere. *J. Atmos. Sci.,* **42,** 1072–1083.

Sutton, R. T., H. Maclean, R. Swinbank, A. O'Neill, and F. W. Taylor, 1994: High-resolution stratospheric tracer fields estimated from satellite observations using Lagrangian trajectory calculations. *J. Atmos. Sci.,* **51,** 2995–3005.

Taylor, F. W., and Coauthors, 1993: Remote sensing of atmospheric structure and composition by pressure modulator radiometry from space: The ISAMS experiment on UARS. *J. Geophys. Res.,* **98,** 10 799–10 814.

Waters, J. W., W. J. Wilson, and F. I. Shimabukuro, 1976: Microwave measurements of carbon monoxide. *Science,* **191,** 1174–1175.

Wofsy, S. C., 1976: Interactions of CH_4 and CO in the earth's atmosphere. *Annu. Rev. Earth Planet. Sci.,* **4,** 441–469.

——, J. C. McConnell, and M. B. McElroy, 1972: Atmospheric CH_4, CO, and $C0_2$. *J. Geophys. Res.,* **77,** 4477–4493.